THESIS

NANOMETER-SCALE MACHINING WITH EXTREME ULTRAVIOLET LASERS

Submitted by

Herman Bravo

Department of Mechanical Engineering

In partial fulfillment of the requirements

For the Degree of Master of Science

Colorado State University

Fort Collins, Colorado

Summer 2013

Master's Committee:

Advisor: Azer Yalin
Co-Advisor: Jorge J. Rocca

Mario Marconi

ABSTRACT

NANOMETER-SCALE MACHINING WITH EXTREME ULTRAVIOLET LASERS

This thesis demonstrates the feasibility of direct machining in the nanometer scale using Extreme Ultraviolet (EUV) laser radiation. Laser machining of materials has been widely used for the development of micromechanical components and devices. Advances in technology further motivate the extension of laser machining of microstructures to smaller dimensions. The advent of high repetition rate table top EUV lasers has opened the possibility of extending laser machining to the nanometer-scale.

It has been previously demonstrated that single laser shots from a 46.9 nm wavelength capillary discharge laser can ablate very clean holes with a diameter as small as 82 nm on polymethyl methacrylate (PMMA) photoresist. This thesis extends previous work by demonstrating nanometer-scale machining of polymers with a focused EUV laser beam. Sub-200 nm wide trenches several micrometers in length were machined on PMMA. These are, to our knowledge, the smallest ablated trenches machined with a focused laser beam.

This work also discusses the study of warm plasmas created by EUV laser irradiation of solid targets in which single-photon photoionization is the dominant energy absorption mechanisms. Low-absorption (silicon, Z=14) and high-absorption (chromium, Z=24, and silver, Z=47) targets were heated by ~ 1 ns duration pulses from a 46.9 nm wavelength EUV laser. The spectra obtained agree with 1 1/2 dimension simulations in showing that the Si plasmas are significantly colder and less ionized, confirming that in contrast to plasmas created by optical lasers the plasma properties are largely determined by the absorption coefficient of the target material.

TABLE OF CONTENTS

CHAPTER 1: EXTREME ULTRAVIOLET ABLATION.

1.1. Introduction.

The processing of materials utilizing various lasers is a rapidly expanding and multidisciplinary field, in which one of the challenges is the development of nanometer-scale devices and structures in high volumes. By virtue of their characteristics, laser beams have been widely used in material processing. These characteristics include, but are not limited to, their high peak power, controlled intensity, short pulse widths, mono-chromaticity, compactness, and repeatability. It is because of these features that for many years, lasers have been widely used for processing in medical, electronic, industrial and material science applications to produce complex shapes with a high degree of robustness, high throughput at low costs.

Industrial efforts have been concentrated in increasing the precision of such techniques in order to achieve smaller feature dimensions. Of interest is the development of laser-based technology that can fabricate 2- and 3-dimensional structures with sizes on the order of several hundred nanometers. These dimensions are fundamental requirements for many applications such as the development of photonic crystals, high density data storage, high resolution displays, optical switches, gratings, integrated circuit devices, metal semi conductor-metal photo detectors, and etcetera.

The very short wavelength of extreme ultraviolet light (EUV) which allows focusing into sub-100 nm spots and shallow penetration depth are significant potential advantages for nano-machining. Therefore, the ablation of materials with focused EUV laser pulses combined with nanometer positioning systems constitutes an attractive approach for the development of new nano-patterning tools with superior control which have great potential for nano-scale machining. I start by discussing different techniques in which ablation takes place when sample materials are

exposed to short-pulses of visible laser radiation. Following is a discussion of ablation of material with EUV light. The chapter concludes with the first demonstration of a new nano-machining technique based on ablation with a focused EUV laser beam.

1.2 Previous Work of Nanometer-Scale Ablation/Machining with Optical Lasers.

For decades, visible short- and ultrashort- pulsed lasers have been used for many large scale industrial material processing applications where concentrated laser beam energy is used in the removal of material through ablation, drilling, cutting as well as other material modifications. The rapid advances in visible lasers development have achieved extremely short pulse widths that can achieve very high pulse intensities using only a small amount of energy. The fundamental advantage of using femtosecond (fs) lasers for nano-machining resides in the fact that short pulse widths limits heat diffusion on the sample material. For example, a pulsewidth of 100 fs and a pulse energy of only 0.33 mJ corresponds to a peak intensity of 10^{15} W/cm^2 when focused to a 20-μm diameter spot, whereas a 10-ns-long pulse would need a 100 J pulse energy to reach the same intensity [1]. In this section I discuss how some of the short- ultrashort pulse visible lasers can play a very effective role in the ablation and sub micron-scale machining of materials.

Microengineering processes play an essential role in the development of many devices. Ultrashort pulsed lasers can process a multitude of solid materials with accuracies and resolutions that range down to that of the wavelength of the laser. In particular, high precision material processing has been demonstrated with femtosecond lasers [1, 2, 3]. In the work by A. Borowiec [3], a study of micromachining grooves on InP with 150 fs, 800 nm laser pulses was performed to characterize ablation rates, geometry and morphology of the machined features.

This research shows that ultrafast laser processing is very promising for materials related to the semiconductor industry.

Selecting the appropriate light pulse for material processing is crucial for achieving the needs desired for manufacturing. The most fundamental feature of material interaction in the long pulse regime is that the heat deposited by the laser in the material diffuses away during the duration of the pulse, as schematically illustrated in Fig. 1.1. This is due to the fact that the laser pulse duration is longer than the heat diffusion time. This may be suitable for applications in the micron scale, but for achieving nanometer-scale precision, heat diffusion into the surrounding material is undesirable.

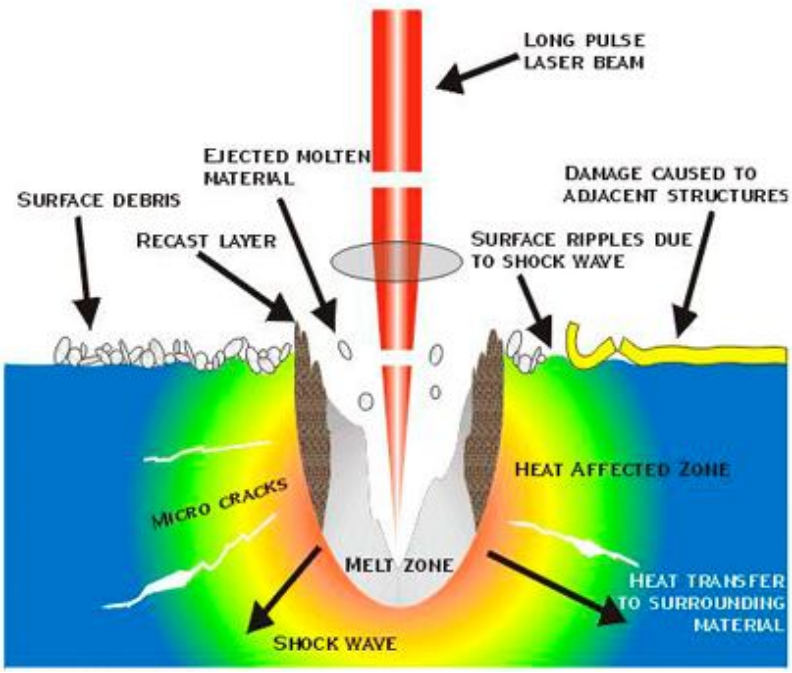

Fig. 1.1 Effects of nano-second laser pulses on materials (Figure from [4]).

M. Jackson and G. M. Robinson [5] *et. al.*, have achieved ablation with visible wavelengths that have produced features ranging from 500 nm to 800 nm in copper, 316 stainless steel and diamond by using a controlled intensity profile, as demonstrated in Fig. 1.2. This process is

performed in such a way that only a fraction of the spot size impinging on the surface is above the threshold energy needed to achieve the desired ablation.

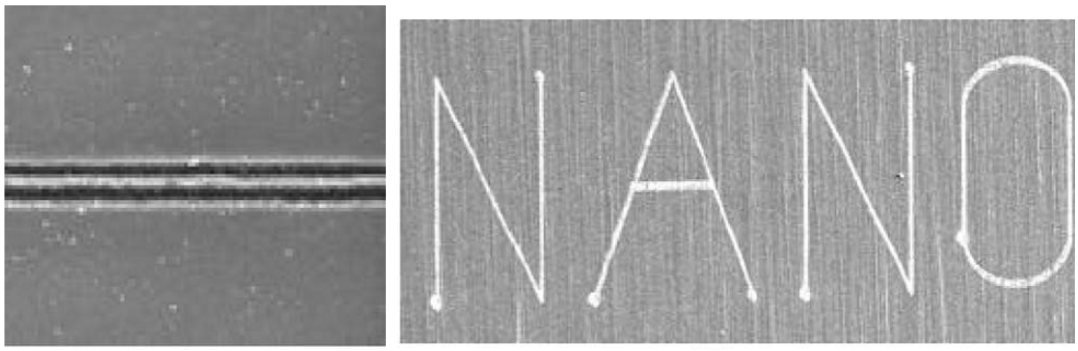

Fig. 1.2 Machining with femtosecond pulsed lasers: (left) 500 nm width lines on copper; (right) 800 nm width lines on steel (Figures from [5]).

Femtosecond visible lasers have been able to achieve precision in micromachining and nanomachining because the ultrashort pulses have precise breakdown thresholds and negligible thermal diffusion. However, features of less than 100 nm have yet to be produced with visible lasers. It is difficult to create nanometer scale features with 800 nm wavelength lasers. The limits presented by the diffraction properties of light ultimately determine the smallest feature resolution possible. Therefore the advantages of visible lasers are found best in the precise ablation in the micrometer scale.

An approach to the production of sub-wavelength lines and structures consists in using femtosecond pulses in combination with a Scanning Near-field Optical Microscope (SNOM). As a possible tool for removing defects, the repair of lithographic masks and nanolithography, S.Nolte [6] *et al.*, have demonstrated the ablation of 200-600 nm wide grooves on a 100-nm chromium layer coated onto a quartz substrate. The group was able to accomplish this with the use of a commercial femtosecond Ti:sapphire laser system (Clark MXR, CPA 2001). Pulses of 1 mJ energy were frequency tripled from 780 nm into 260 nm pulses with energy of 0.1 mJ. The

radiation produced was coupled into a hollow fused-silica micropipette with a chrome coating. The micropipette, shown in Fig.1.3A, had an inner tip diameter of the order of 500 nm with a tip angle of 20° and was placed 50 nm above the sample surface. The grooves were produced on a chromium surface by scanning of the sample at two different velocities: 2 μm/s and 10 μm/s. The cross sections of the ablated grooves are shown in Fig. 1.3B. The width of the left groove is approximately 600 nm and that of the right groove is 200 nm. The authors note that the laser pulse energy has a Gaussian spatial distribution.

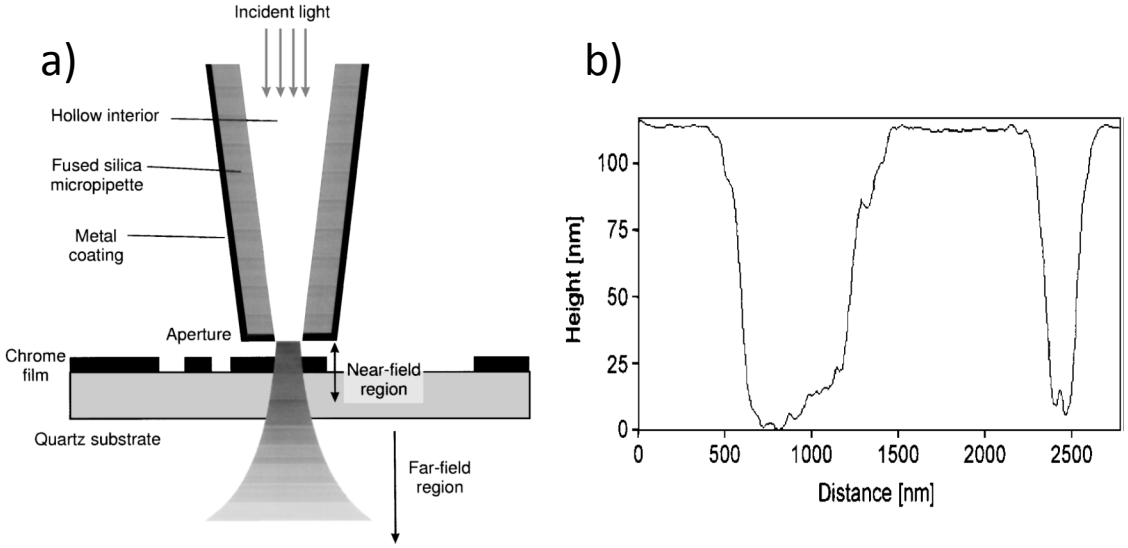

Fig. 1.3 (A) schematic diagram of the experimental SNOM set up. Fig. 1.3 (B) AFM image of a cross section of two ablated grooves produced in chrome by scanning of the sample at speeds of 2μm/s (left) and 10 μm/s (right) (Figures from [6]).

Such a laser tool has potential for industrial applications as it can play an important role in dicing, prototyping, trimming and device repair as shown in Fig. 1.4.

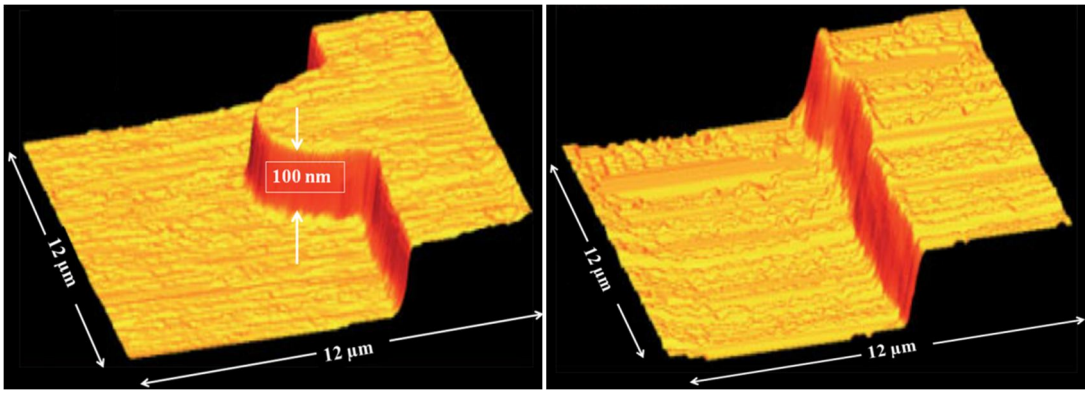

Fig. 1.4 AFM topographical images of (left) programmed defect and (right) the repaired site. The height of the chromium layer upon the quartz substrate is approximately 100 nm (Figures from [6]).

There exist several other optical approaches that overcome the diffraction limit to enable machining in the micron width as well as down to the nanometer scale. The multiphoton absorption (MPA) method and the electron avalanche ionization process are both vital phenomena that enable the diffraction limit of laser light to be overcome in order to ablate below the micron scale. The multiphoton absorption process, illustrated in Fig. 1.5, is one in which two or more photons are simultaneously absorbed by an atom. An atom, through this phenomenon, will absorb several infra red photons and react as if it had absorbed a ultraviolet photon. When the laser field strength impinging on the material is high enough, the bound electrons of the material are directly ionized. The bound electrons are ionized when simultaneously absorbing n photons from the laser pulse i.e. $n \cdot h\nu \geq U_I$ where U_I is the ionization potential and $h\nu$ is the energy of a photon with wavelength $\lambda = c/\nu$.

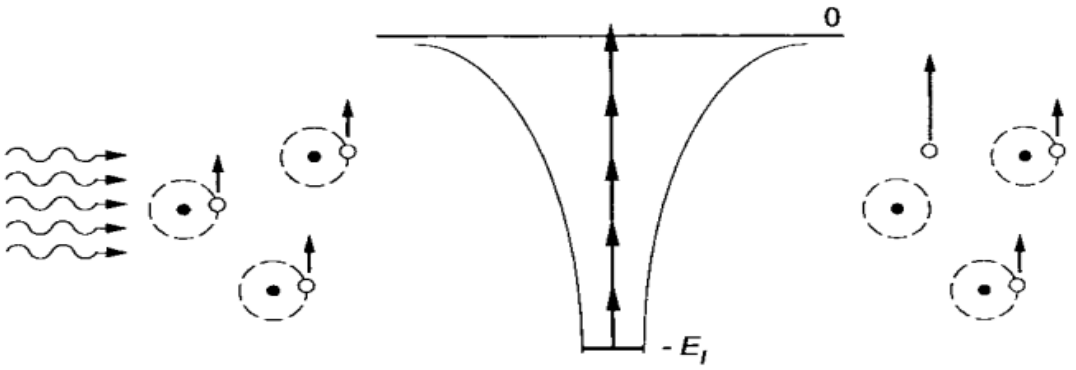

Fig. 1.5 Schematic representation of the Multiphoton Ionization Process. The bound electrons in the atom are ionized when absorbing n photons with wavelength λ. This is an effective way to overcome the diffraction limit (Figure from [1]).

Multiphoton ionization is only effective when the electric field impinging on the material is sufficiently strong. Therefore, multiphoton ionization typically takes place at ultrashort pulse-widths [1].

The ability to create structures on the micro- and nano-scale with visible lasers is strongly dependent on the pulse-width of the laser beam. Because of this important constraint, beams with long wavelengths and long pulse-widths are unsuitable tools for nano-machining due to the extensive heat diffusion into the material. On the other hand, short pulsed lasers with long wavelengths can still be effective in creating microstructures as heat conduction in the material is strongly limited resulting in a clean ablation process as the absorption depth becomes greater than the laser diffusion length which leads to the localization of energy. Consequently, this process causes direct vaporization of the material resulting in high precision ablation as illustrated in Fig. 1.6.

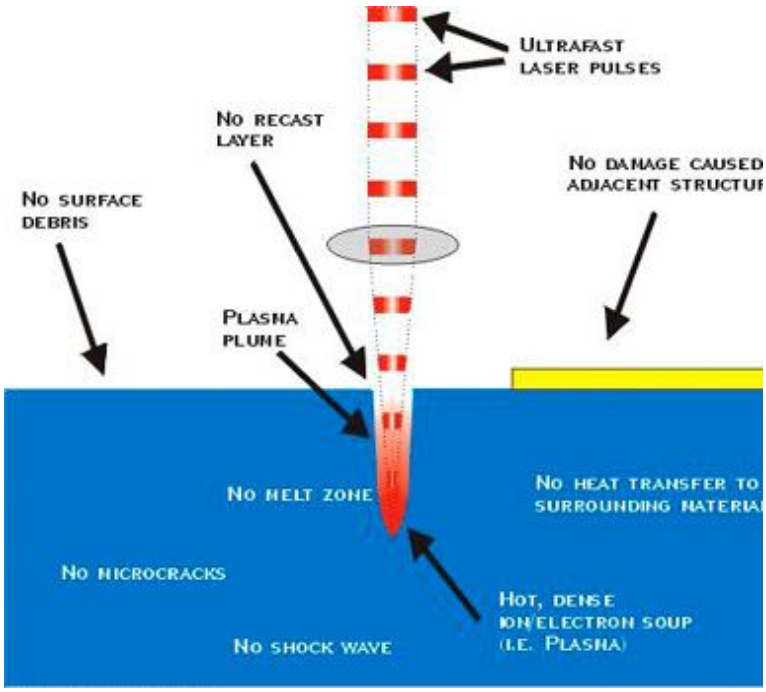

Fig. 1.6 Effects of femtosecond laser pulses on materials (Figure from [4])

By combining femtosecond laser pulses with SNOM, nanostructures can be developed by overcoming the diffraction limit and can be fabricated in atmospheric conditions. Improved design of SNOM fiber tips can increase the light throughput which can extend to more ablation applications. Fig. 1.7 shows a 20 nm trench ablated on ma-P (Micro Resist Technology) photoresist. To date, this process has achieved feature sizes close to 20 nm [7]. S. Nolte *et al*., notes that these feature sizes are comparable to electron-beam lithography and can be used for ultrahigh-capacity data storage and new functional nano-device fabrication.

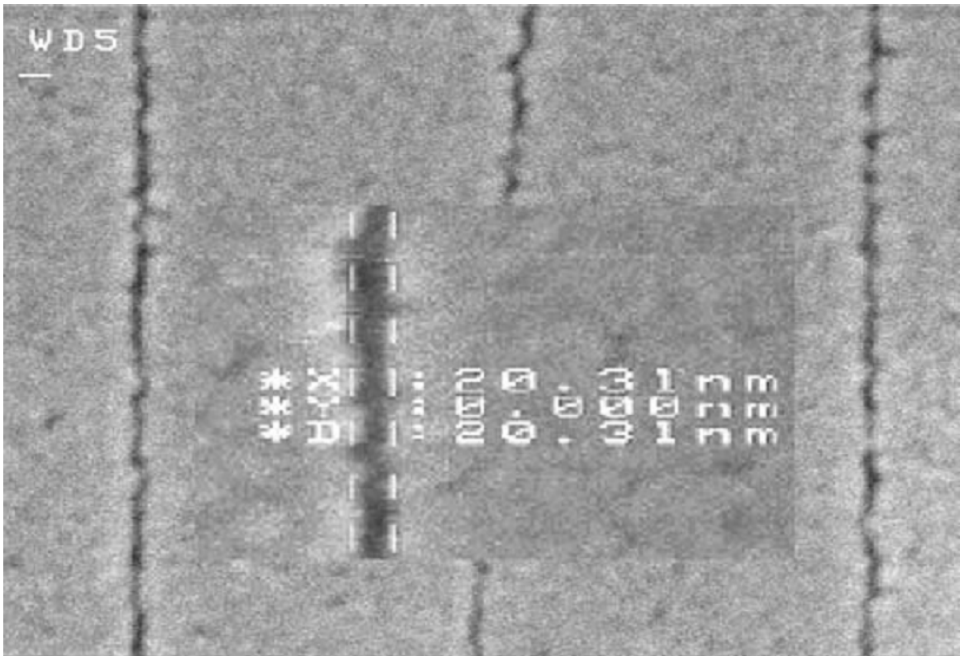

Fig 1.7 20 nm wide line machined on photoresist by SNOM Microscopy [Figure from [7]).

1.3 Ablation and Machining with Ultraviolet Lasers.

Ablation of organic polymers by optical radiation, in particular from excimer lasers, has been extensively studied. Ablation performed by excimer lasers in the UV range has been shown to be a viable technique for micro-fabrication as it can be used to machine a variety of materials without the need for a sacrificial layer [8]. It has been shown by Avrutsky *et al.* that "super-resolution" (feature diameter less than a micron) in laser ablation was achieved when they used a KrF laser (Lambda Physik LPX 205) and focusing the radiation onto a 5.6 μm diameter spot. As seen in Fig. 1.8, super resolution was observed on films of Si/silica and Al/glass where the heat diffusion length $\sqrt{\sigma_f \tau}$ is 1.5, 1.4, and 0.10 μm for Al and Si, where σ_f is the thermal diffusivity of the film and τ is the pulse duration of 25 ns.

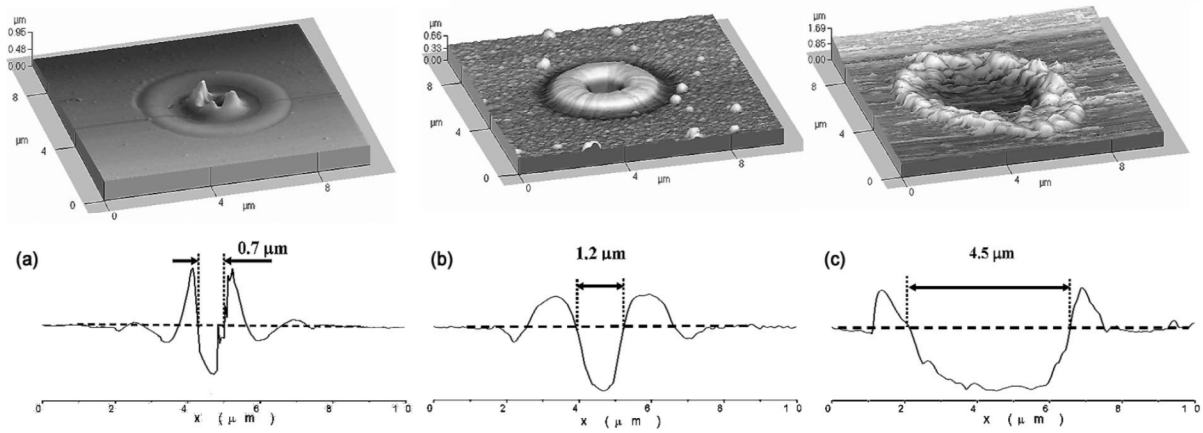

Fig 1.8 AFM three-dimensional image and the surface profile of samples ablated with an UV excimer laser. (a) 200 nm silicon-on-silica film after ablation by a single pulse at 2.5 J/cm^2; (b) 200 nm aluminum on-glass film after ablation by a single pulse at 2.1 J/cm^2; (c) 356 nm TiO_2–SiO_2 -on-glass film after ablation by a single pulse at 2.5 J/cm^2 (Figures from [8]).

The authors report that ablated holes with "super-resolution", dimensions were formed when the laser fluence was 10-20 percent above the ablation threshold. The resulting laser ablated features were eight times smaller than the diameter of the irradiated spots. They conclude that when using materials with high thermal conductivity, effectively choosing laser fluence and processing geometry allows for a better spatial resolution of the ablated features and speculate that a tightly focused laser beam (e.g. diameter smaller than 0.5µm) can be ultimately used to ablate features less than 100 nm in resolution.

P.E. Dyer *et al.* [9] noted that industrial applications for the 157 nm vacuum ultraviolet F_2 laser will increase as the lasers performance improves with the advancements in beam delivery optics. As such, this VUV laser system has proven to be highly adept as an ablative instrument when trying to achieve high resolution machining. Fig. 1.9 demonstrates how an F_2 laser can machine high quality lines on

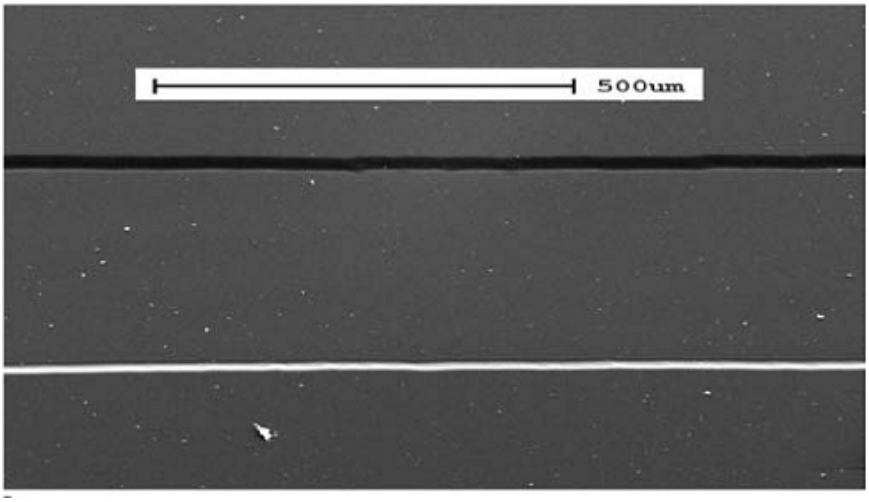

Fig. 1.9 Long micron-width channel on PMMA ablated using a 157nm F_2 laser. The image shows a smooth and clean processed surface. The width of the channel is several hundred nanometers (Figure from [9]).

a sample of Polymethyl methacrylate (PMMA) with no significant thermal damage to the surrounding surface and demonstrates its strong ability to pattern long micrometer width channels .

In 1997, research with ultraviolet lasers was performed to investigate the ultimate resolution achievable on metal and semiconductor samples. These findings helped to define the experimental conditions needed for high quality machining in materials. In research done by P.Simon *et al.* [10], individual holes were ablated on sample surfaces with the use of a short pulsed KrF-laser at 248 nm with a 10 mJ pulse and a Schwarzchild objective. Periodic structures with 364 nm widths were ablated on copper when a transmission grating was imaged onto the samples though a Schwarzschild objective. Each image was generated with a single pulse from a KrF-laser system producing pulses of 248 nm at an output of 10 mJ. Fig. 1.10 shows the ablated lines with pulse durations of 500 fs, 5ps and 50 ps. To date, these ablated lines have the smallest widths achieved through ablation with an ultraviolet radiation source.

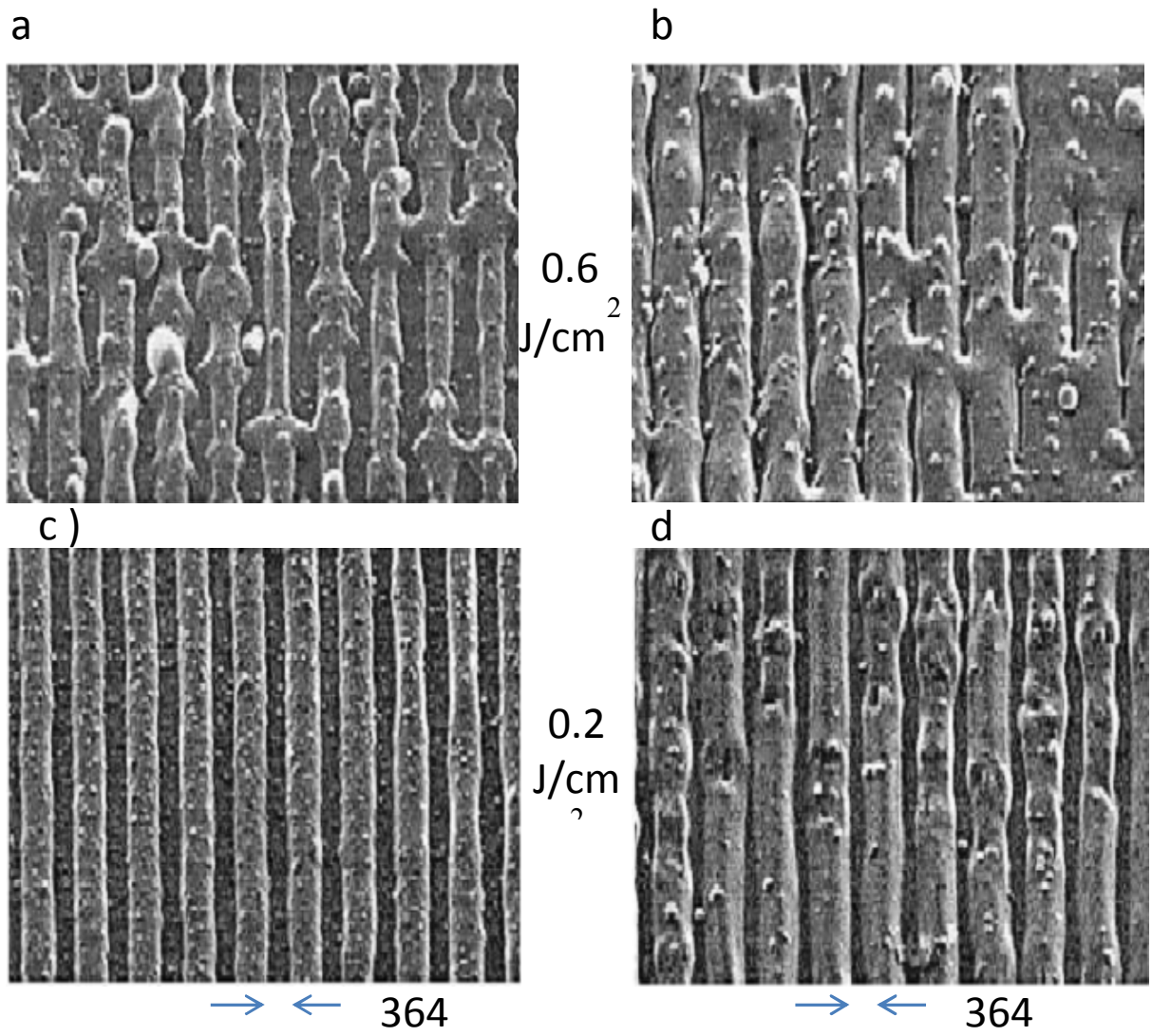

Fig. 1.10 Periodic structures ablated on silicon samples. Each image was generated with a single pulse from a KrF-laser system producing pulses of 248 nm at an output of 10 mJ . Each image was ablated with a different pulse duration and fluence: a) 5 ps, 0.6 J/cm^2 , b) 50 ps, 0.6 J/cm^2 , c) 5 ps, 0.2 J/cm^2, d) 50 ps, 0.2 J/cm^2 (Figure from [10]).

1.4 Previous Ablation Work with EUV and X-ray Radiation.

The wavelength range of EUV and soft X-Ray (SXR) radiation is not precisely defined. However, it is often considered that EUV light has photon energies from 25 eV to 250 eV, corresponding to wavelengths extending from 50 nm to 5 nm, while the soft x-ray region is defined to extend from photon energies of 250 eV to a few keV, as illustrated in Fig.1.11. This

region of the electromagnetic spectrum has not yet been fully exploited due to limited availability of intense compact light sources [14].

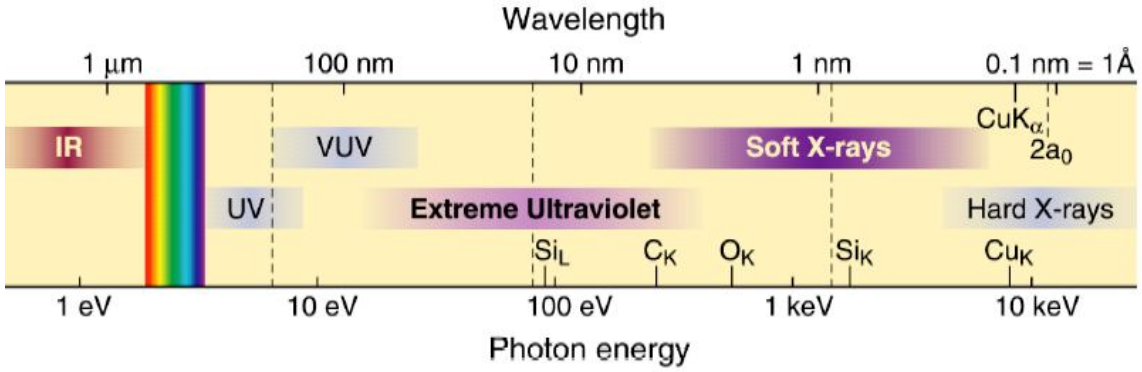

Fig. 1.11 The electromagnetic spectrum from the infrared to hard X-rays (Figure from [14]).

EUV and SXR radiation has been used in the removal of solid material in micro- and in nano-structuring/patterning. The photons emitted from EUV and SXR radiation sources carry enough energy to break chemical bonds in the sample material. This energy is also higher than the cohesive energy of any crystal. In experiments where low-peak-intensity EUV radiation is used, most of the material removed from the sample comes mainly from a very thin, near-surface layer. Experiments where high-peak-power sources deliver high-energy pulses onto the sample have a different outcome: the sample is exposed to a high dose of radiation in a short period of time. The impinging radiation produces structural decomposition, like polymer chain scissions, to occur simultaneously on the sample surface. The irradiated material, now chemically altered by the radiation, is ejected from the surface of the material and off into the vacuum.

In experiments by L.Juha, *et al.* [12], PMMA ablation was demonstrated by optimized EUV and SXR short pulse radiation. The PMMA samples (500 nm thick layers of 495 K PMMA coated on Si chips) were placed behind masks of either a nickel mesh of 20/30 μm wires or a 25 nm thick Si_3N_4 window. The EUV/SXR radiation was emitted by either a Z-pinch plasma or a

plasma produced by focusing a near-infrared laser onto a surface of a planar metal-slab target. By varying the parameters of the two radiations sources, a wide variety of photon energies, pulse duration, and energies were used to test ablation parameters on PMMA and Teflon (PTFE) samples. The results of the trials are shown in Fig. 1.12.

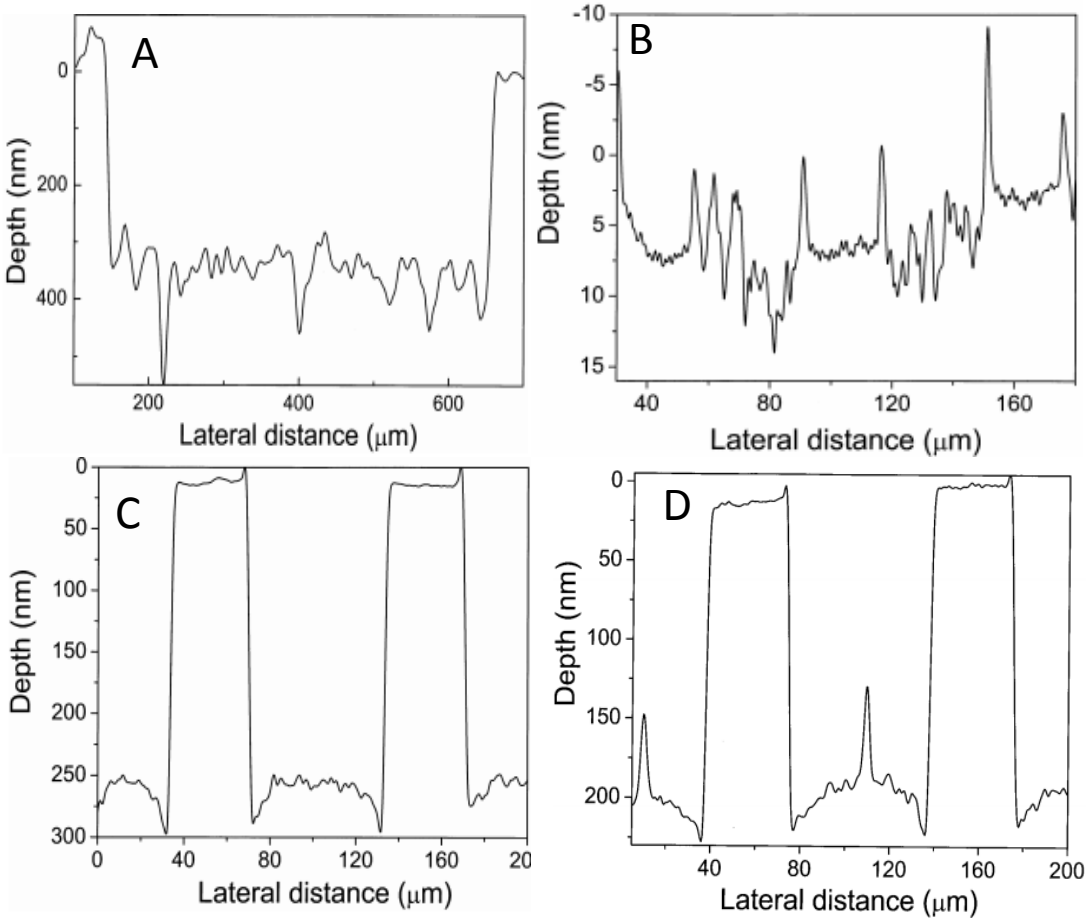

Fig. 1.12 Profile depths of PMMA films ablated with EUV/SXR radiation measured with an Alpha-Step 500 surface profiler. A) Ablation of a 1-mm-thick PMMA sample irradiated by an EUV/SXR pulse from a Z-pinch plasma delivered through a Si_3N_4 window. B) PMMA sample irradiated through a nickel mesh by EUV/SXR radiation from molybdenum plasma produced by a tight focusing of laser radiation on the target surface C) The PMMA sample irradiated through a nickel mesh by an EUV/SXR pulse emitted from Z-pinch plasma D) Ablated samples exhibiting hydrodynamic character centered in the radiated region (Figures from [12]).

When irradiated with EUV/SXR radiation from a Z-pinch plasma through a Si_3N_4 window, ablation of PMMA was demonstrated and resulted in clean structures. A trench approximately 350 nm deep is shown in Fig. 1.12A. The EUV radiation intensity impinging on the sample

surface was in the range of MW/cm^2 and was produced by a Z-pinch plasma with a W liner / C wire at a current of 2.1 MA. By increasing the distance between the sample and the discharge plasma from 11.5 cm to 15.5 cm, a decrease in the ablation efficiency was demonstrated as only a few nanometers of the sample surface was ablated. Other surfaces raised by bubbles appeared on parts of the surface where the fluence is near the ablation threshold (Fig. 1.12B). When the radiation source is driven by an Al liner with a central C wire, deep and clean structures on PMMA were obtained (Fig. 1.12C). Under the same conditions for ablation, hydrodynamic characteristics of the PMMA sample are exhibited as small peaks were formed in the center of the ablated region (Fig. 1.12D). The authors suggest that those peaks are relics of hydrodynamic transport of "fluid" formed from the polymer chains that have undergone through multiple radiation scissions, heated by EUV/SXR radiation [12].

The rapid development of new intense, coherent short-wavelength pulse sources, like the compact capillary discharge laser used in this thesis and the EUV Tesla/FLASH Free Electron Laser (FEL) at DESY in Hamburg, open up new possibilities for material ablation research. The FELs are advanced radiation sources that can emit very high fluxes in the EUV and X-ray spectral regions [12]. Due to the recent availability of such facilities, new studies were conducted to fully understand the interaction of the intense, ultra-short EUV pulses with materials. These studies have helped to predict performance and lifetimes of materials applicable to work under the extreme load generated by the FEL beams. Recently, damage morphology in samples of Si (001) due to exposure from the EUV TESLA FEL was reported [14]. By irradiating targets with EUV energy, it is expected that the ablation process would be different from those of ultra-short optical laser pulse irradiation. In an experiment by L. Juha *et. al.* [14], irradiation of solid targets was carried out with EUV pulses with duration of 50-100 fs

generated at the TTF EUV FEL. The laser was tuned to a wavelength of 88.6 nm (14eV) and the average pulse energy was about 10 μJ. Figure 1.13 shows 7 ablated regions where the sample was irradiated with 11 pulses at a repetition rate 1 Hz. The ablated areas were distributed over the sample surface in nodes of a 150–300 μm mesh grid.

The data obtained demonstrates that the patterns ablated on Si(001) have similar features to that of surface structures irradiated with optical light sources. However, it is noted that the patterns created with the EUV radiation have rich details, as fine as a few nanometers in scale. These results support the author's opinion in assuming the strong localized interaction of EUV FEL pulse radiation energy with solids [14]. To this date, no nanometer scale features have been ablated using EUV FEL's.

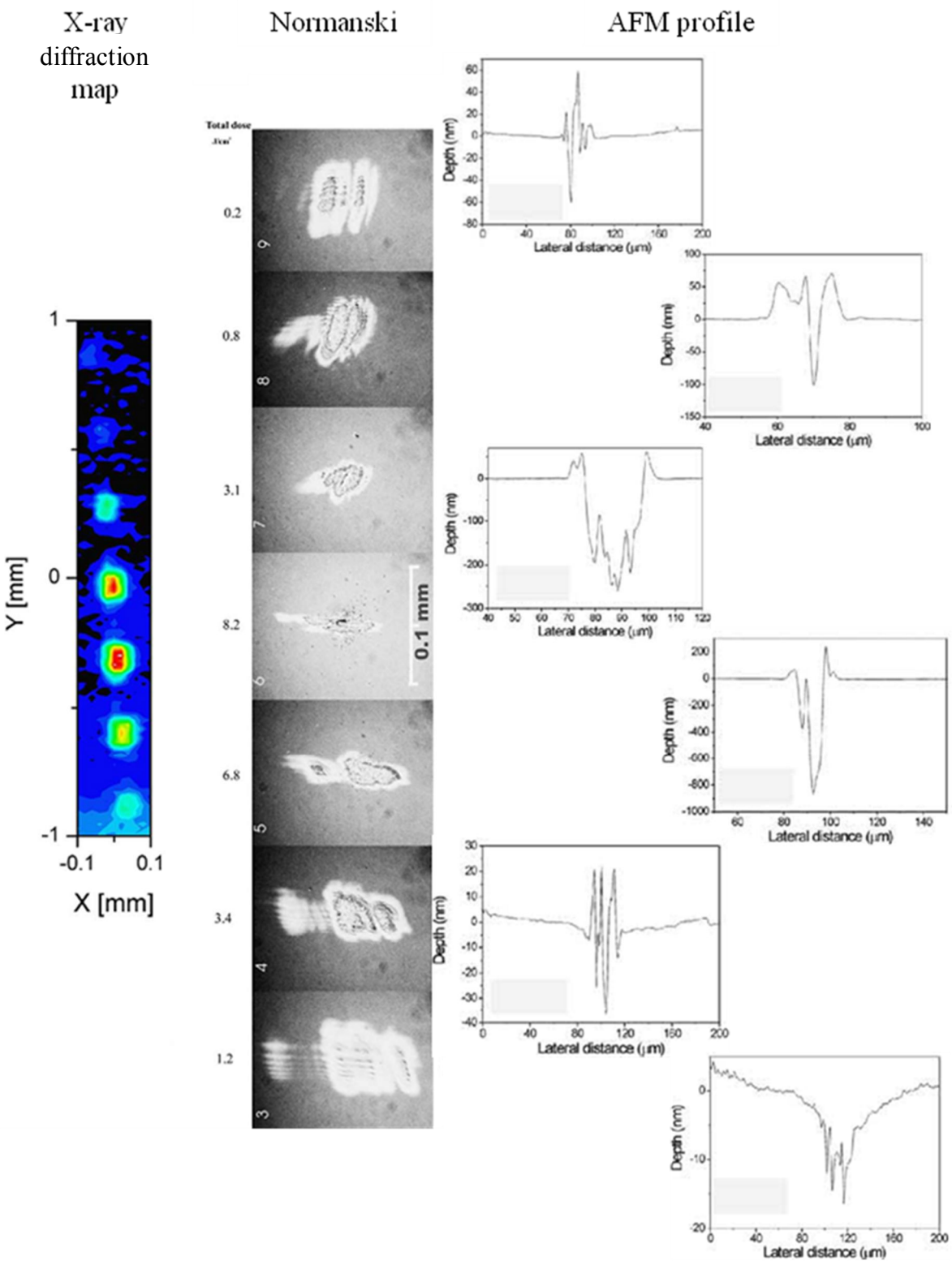

Fig. 1.13 Ablation results from an experiment at the TESLA EUV FEL. Left: Si(400) X-ray diffracted intensity distribution maps around the spots; Center: Nomarski contrast microscopy pictures from 11 shots each; Right: AFM profiles. (Figures from [14]).

1.5 Previous Work of Nanometer-Scale Ablation with an EUV Laser.

It was previously demonstrated that single EUV radiation pulses from a 46.9 nm wavelength capillary discharge laser can ablate very clean holes with diameter as small as 82 nm on photoresist [17]. Research in this thesis extends this result demonstrating the feasibility of performing nano-scale machining of polymers by using focused EUV laser beams. The ablation of sub-200 nm wide trenches several micrometers in length on PMMA was achieved.

In previous work the output from a compact $\lambda = 46.9$ nm capillary discharge laser [18] was focused with a free-standing zone-plate (FZP) lens to ablate craters with very clean walls in PMMA. By varying the position of the FZP with respect to the target sample, a variety of craters with varying diameters and depths were produced. Figure 1.14 illustrates the experimental set up. The laser output for a 18.1 cm long capillary discharge, consisting of 0.1 mJ pulses of 1.2 ns duration, was focused onto the sample's surface with a FZP lens forming a diffraction limited focal spot size of 240 nm in the first diffraction order. A laser pulse energy of 10 μJ was measured through a 6 mm pinhole placed at the location of the FZP using a gold vacuum photodiode. The fluence onto the sample was controlled by introducing argon gas in the vacuum chamber and by adjusting its pressure as a mean to attenuating the laser pulse energy. The FZP used in this experiment had a 0.5 mm diameter, an outermost zone width of 200 nm, and a numerical aperture (NA) for the first diffraction order of 0.12.

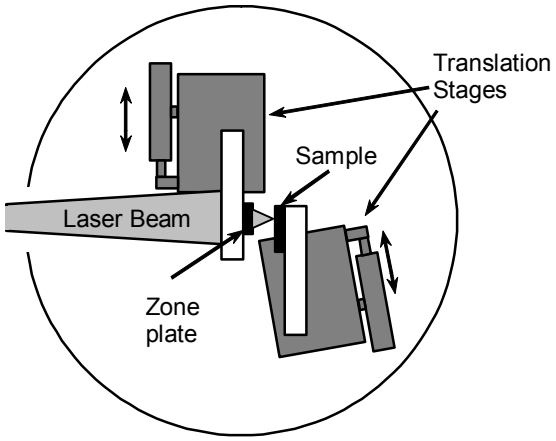

Fig. 1.14 Schematic diagram of the EUV laser ablation set up. The laser beam enters the chamber through the port on the left; it is focused by a zone plate onto the sample. The translation stages can place the sample at either 1st or 3rd order diffraction focus of the zone plate lens (Figure from [17]).

The sample was positioned approximately 1.8 m from the laser output where the laser beam has a full width at half maximum diameter of 16 mm. The samples consisted of a thin 100 nm thick layer of PMMA (MicroChem, 950,000 molecular weight) deposited onto a silicone wafer using a standard spin coating techniques.

As seen in Fig.1.14, the FZP was mounted on an XYZ translation stage. The samples were positioned perpendicular to the incident EUV laser beam, whereas a translation stage tilted at an angle of 0.57º with respect to the sample's surface allowed for the precise positioning of the sample at the FZP's focal plane (first order depth of focus 3 μm). The ablation craters produced by a single laser pulse from the $\lambda = 46.9$ nm laser beam were analyzed with a VEECO NanoScope III atomic force microscope (AFM) used in tapping mode with a 10 nm radius, 30º cone angle cantilever tip (MicroMasch, NSC16).

Techniques were implemented to find the best focus for ablating the smallest craters. The first technique involved placing the sample 100 μm away from the best calculated focus. The

sample was translated towards and normal to the calculated focus as the laser was fired at 1 Hz. This ensured that the laser always impinged on a new target area.

Figure 1.15 shows an AFM image of a 300 nm diameter ablation hole which was obtained by placing the sample at the first diffraction order focal plane of the zone-plate. Smaller holes were achieved by placing the sample at the third diffraction order focal plane of the lens.

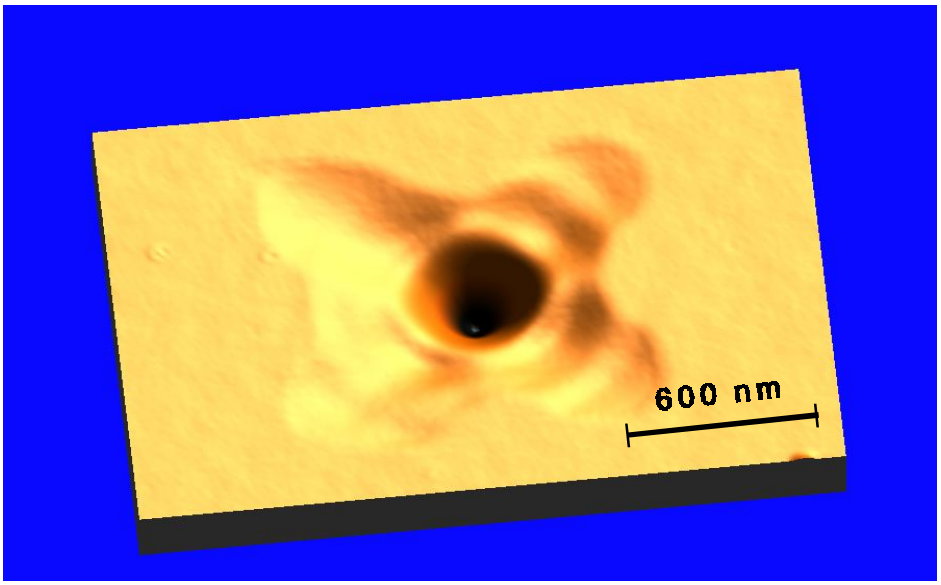

Fig. 1.15 AFM image of the ablation crater produced focusing a 46.9 nm laser pulse on PMMA in first diffraction order. The crater is approximately 300 nm in diameter. The laser beam was attenuated by 36× (Figure from [17]).

To gain insight on the characteristics of the beam profile generated by a FZP, the intensity distribution in the third order focal plane was simulated solving the Rayleigh-Sommerfeld diffraction integral. The simulation result depicted in Fig. 1.16 shows that the intensity distribution at the third order diffraction focus consists of a broad peak with a FWHM of 270 nm.

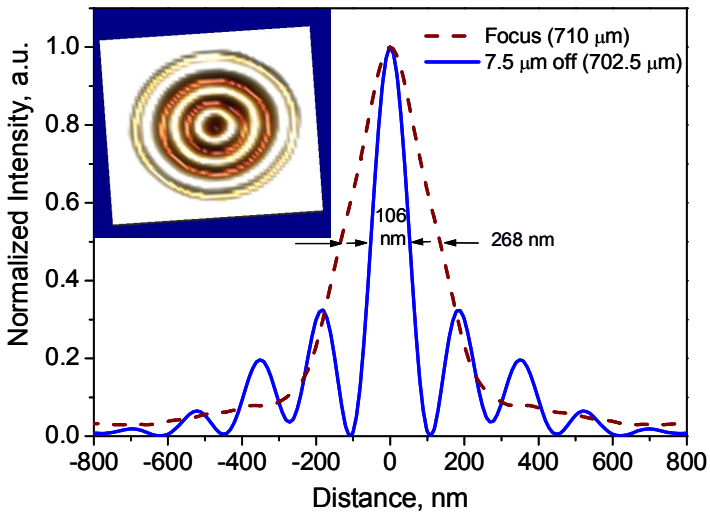

Fig. 1.16 Intensity distribution at the third order focal plane simulated using Rayleigh-Sommerfeld diffraction at the focus and 7.5 μm away from the focus (Figure from [17]).

However, at a plane several micrometers away from the third order focal plane the simulation predicted an intensity distribution (also shown in Fig. 1.16) consisting of a narrow central peak, 100 nm FWHM, surrounded by a set of concentric lower intensity rings. These results were confirmed experimentally by ablating a PMMA coated Si-wafer placed at 7 μm away from the third order focal plane. An AFM image of the structured light intensity distribution transferred to the PMMA is shown in the inset of Fig. 1.16. The rings were attenuated to intensities below the ablation threshold of PMMA by introducing argon gas into the processing chamber, therefore allowing the use of the central intensity peak for small scale ablation.

Figure 1.17 shows an AFM image of the smallest ablation craters, 82 nm in diameter, obtained in PMMA by placing the sample at the third order focus of the FZP. The shot to shot reproducibility of the ablation was found to be very good.

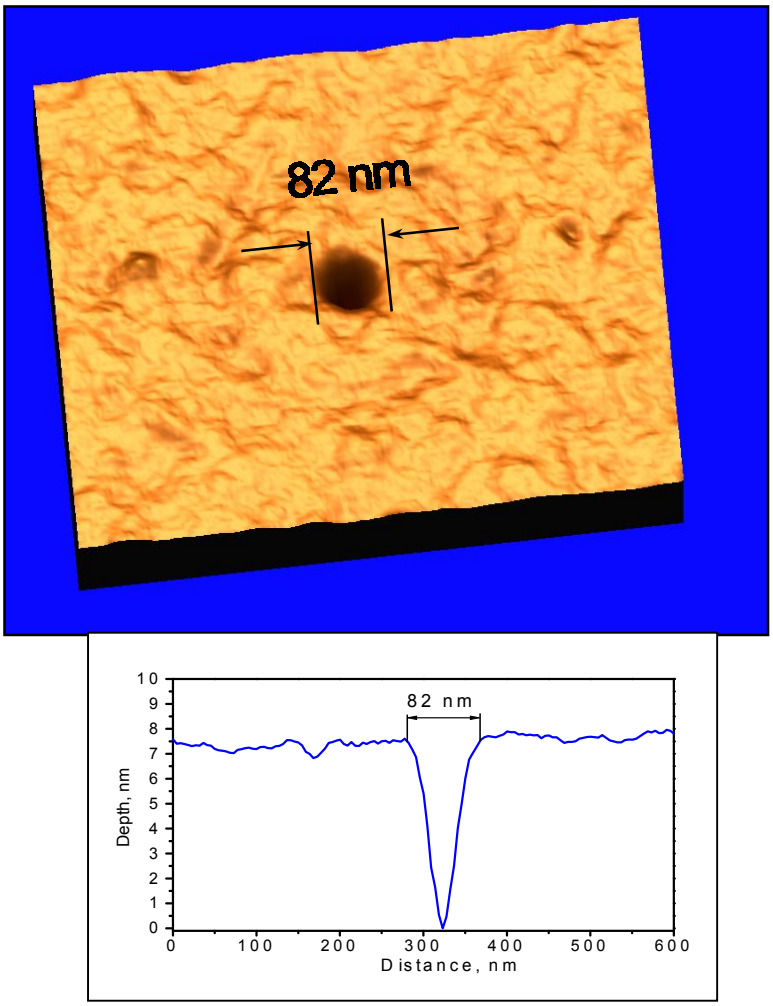

Fig. 1.17. AFM image of an 82 nm diameter crater obtained placing the sample ~7 μm away from the third diffraction order focal plane. The inset shows the crater's cross section (figures from [17]).

The holes obtained with single laser shots in this way have very clean walls. These results demonstrated the ability to ablate sub-100 nm holes with a focused EUV laser beam. These are the smallest ablation holes obtained to date by direct focusing of an EUV laser beam onto a sample.

CHAPTER 2: EUV LASER NANOMETER-SCALE MACHINING.

This chapter describes the EUV nanometer-scale machining set up developed as part of this thesis and the results obtained. It describes how different components were assembled to obtain the nanometer-scale machining results. It begins with a description of the Neon-like Argon laser used as the illumination source. Following this initial section, a description of the diffractive optics used to focus the EUV laser beam is provided. Next a description of the setup that was used to realize ablation in the first and third order focal planes of a Fresnel zone plate lens is provided. The chapter ends with AFM images of nanometer-scale trenches ablated on PMMA.

2.1 Description of the 46.9 nm Capillary Discharge Laser.

The EUV ablation set up uses a table-top capillary-discharge laser as the illumination source. This EUV laser, developed at Colorado State University by J.J. Rocca and colleagues [18], emits at a wavelength of 46.9 nm with a 1.2 ns pulse duration and has a spectral bandwidth of $\Delta\lambda/\lambda<1\times10^{-4}$ [19- 20]. The output of this collisional-excitation laser is produced by a population inversion between the 3p and 3s (J = 0 to 1) line of Ne-like argon at 46.86 nm.

To generate the gain medium, an aluminum oxide (Al_2O_3) capillary with inner diameter of 3.2 mm and high aspect ratio (>1:50) is filled with 0.5 Torr of argon. Population inversion is produced exciting the gas with 24 kA current pulse with a 10 percent to 90 percent rise time of 25 ns and a first half cycle duration of 110 ns [19]. The flow of the current pulse through the capillary induces a magnetic field which through the Lorentz force rapidly compresses the plasma into a hot and dense plasma column with a diameter of 200-300 μm, where the laser pulse is produced. This compression heats the plasma creating plasmas columns with aspect

ratios higher than 1:600 with the necessary conditions for lasing. The heated electrons ionize the argon atoms eight times to the Neon-like state and excites the ions by collisional electron impact excitation creating a population inversion. The 46.9 nm light is amplified exponentially until gain-saturation is reached, after which the laser pulse energy increases linearly with plasma column length.

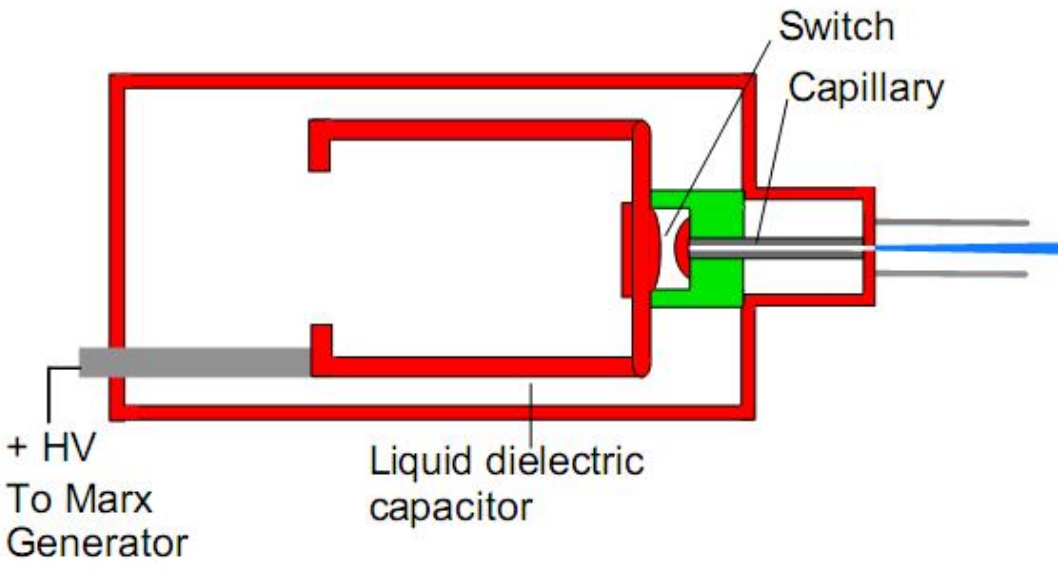

Fig. 2.1 Schematic diagram of the capillary discharge table top extreme ultraviolet laser.

To create the fast current pulse a 3 nF water capacitor is discharged through a spark gap switch connected in series with the capillary [19]. The capacitor is charged to 200 kV by a four-stage Marx generator. The Marx generator is safely enclosed in a separate box and connected to the laser discharge head through a high voltage coaxial cable. The water in the capacitor serves as dielectric as well as a coolant for the alumina capillary. The laser output pulse energy and degree of spatial coherence depend on the capillary length. For most of the experiments, Al_2O_3 capillary lengths of 27 cm were used. The 27 cm capillary, when fully optimized can provide an output energy of up to 0.4 mJ / pulse. However, values of 0.1 to 0.2 mJ/pulse are more typical in

day-to-day operation. The choices of capillary lengths were made to ensure sufficient photon flux to ablate the surface of PMMA.

Figure 2.2 shows two-pinhole interferograms which depict the degree of spatial coherence and as a function of capillary lengths [21]. The fringe visibility is related to the degree of spatial coherence. From the figure it is clear that the degree of spatial coherence increases greatly with capillary length. In contrast to the 18 cm capillary, the output of the 36 cm long capillary plasma columns is highly coherent. The shortest, 18 cm long capillary, produces a low coherence output. This property of the capillary discharge laser allows to tailor the degree of spatial coherence by selecting the appropriate capillary length.

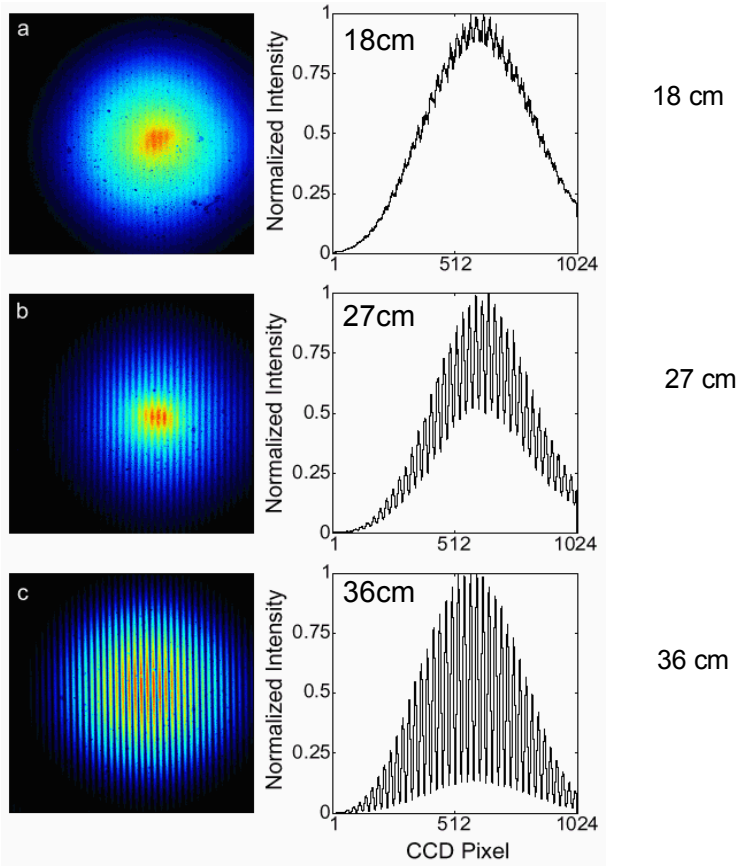

Fig 2.2 Interferograms and corresponding lineouts showing the coherence buildup of the laser beam with increasing capillary length. The capillary lengths are (a) 18 cm, (b) 27 cm, (c) 36 cm. (Figures and data from [21]) .

2.2 Diffractive Optics -Fresnel Zone Plate Lenses.

The laser beam used in the ablation experiments is focused using diffractive optics, known as Fresnel zone plates (FZP). There is an extensive literature that treats this subject. I will follow the treatment in the text "Soft X-rays and Extreme Ultraviolet Radiation" by D. T. Attwood [15] to derive the formulas that describe the characteristics and performance of the Fresnel zone plates. A Fresnel zone plate is schematically illustrated in Fig. 2.3.

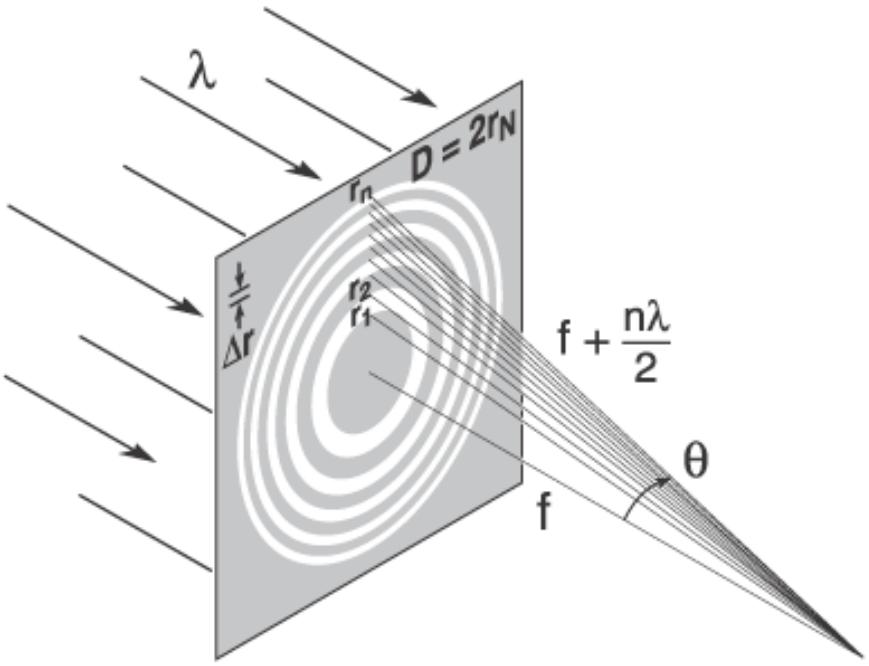

Fig 2.3 Representation of Fresnel zone plate lens with plane wave illumination, showing only the convergent 1st order of diffraction. Sequential zones of radius r_n are specified such that the incremental path length of the focal point is $n\lambda/2$. Alternate zones are opaque in the simple transmission zone plate. (Figure from [15]).

Diffraction is the process by which radiation is redirected off of sharp edges. When combined with repetitive structures that contain arrays of parallel lines and spacing, a strong redirection of radiation can be achieved. A Fresnel zone plate can be envisioned as a circular transmission grating which has a proper placement of radial zones to produce positive

interference of the diffracted light in a well-defined downstream position. Figure 2.3 shows a zone plate illuminated by a plane wave. With the use of the geometry shown, the impinging wavefront can converge onto a point at a focal distance *f*, for the first order of diffraction.

The radii of sequential zones are chosen such that the incremental path length to the focal point is nλ/2. Constructing a triangle for the n^{th} zone and using the Pythagorean theorem the radius of any zone is found as:

$$r_n^2 = n\lambda f + \frac{n^2\lambda^2}{4} \qquad (1)$$

where n is the is the zone number being considered and λ is the radiation wavelength. The term $n^2\lambda^2/4$ represents spherical aberrations. Since we are dealing with extreme ultraviolet wavelengths, where $\lambda/(2\Delta r) << 1$, the term $n^2\lambda^2/4$ can be dropped for cases where $f >> n\lambda/2$ (as for a lens with small numerical aperture) . Expression 1 can then be reduced to

$$r_n \approx \sqrt{n\lambda f} \qquad (2)$$

which shows that the zone radius must increase by $\sqrt{n}$ in order to achieve a real first order focus. However, in order to diffract radiation to a common focus, the width of consecutive zones must decrease as they approach the periphery of the zone plate. This will create a circular grating structure of decreasing period (i.e. one set of consecutive opaque and transparent zones).

The outer zone width of the zone plate can be obtained by subtracting the radius of the *N-1* zone to the radius of the N^{th} zone, where *N* is the total number of zones in the zone plate including the transparent and opaque zones.

$$\Delta r \equiv r_N - r_{N-1} \tag{3}$$

To derive an expression for the diameter of a zone plate we write using eqn. 1:

$$r_N^2 - r_{N-1}^2 = N\lambda f - (N-1)\lambda f = \lambda f \tag{4}$$

The left side of eqn. 4 can be rewritten as:

$$r_N^2 - (r_N - \Delta r)^2 = 2r_N \Delta r - (\Delta r)^2 \approx 2r_N \Delta r \tag{5}$$

Then

$$2r_N \Delta r \approx \lambda f \tag{6}$$

Realizing that $2r_N$ is the diameter, *D*, of the zone plate and combining eqn. 2 and 6 one obtains an expression for the diameter of the zone plate in terms of the outer zone, Δr, width and the number of zones, *N*:

$$D = 4N\,\Delta r \tag{7}$$

From eqn. 6 and 7 the focal length for the first order of the lens can be obtained:

$$f \approx \frac{4N(\Delta r)^2}{\lambda} \tag{8}$$

Eqn. 8 shows three important features regarding the focal length of a FZP. The first is that the focal length has a high chromatic dependence to the inverse of the wavelength impinging on it. To avoid chromatic aberration, the spectral bandwidth must satisfy the relation $\frac{\Delta\lambda}{\lambda} \le \frac{1}{N}$. The narrow linewidth of the 46.9 nm Ne-like Ar capillary discharge extreme ultraviolet laser is therefore an advantage for the use of this laser in combination with FZPs.

Second, the focal length is highly sensitive to the square of the outer zone width, which essentially sets the resolution limit of a zone plate imaging system. Lastly, the focal length is scaled directly to the total number of zones on the plate.

In the paraxial (small angle) approximation, the numerical aperture (NA) of the FZP is given by the ratio of the radius of the Nth zone over the focal distance, *f*. Equivalently, by combining eqn. 7 and 8 we can obtain the numerical aperture of the lens in terms of the outer zone width:

$$\mathrm{NA} = \frac{\lambda}{2\,\Delta r} \tag{9}$$

An important parameter for ablation experiments is the depth of focus (DOF), Δz. The DOF defines the range at which the optics can be displaced away from the focal spot without significantly reducing the intensity. It follows that the DOF, used from reference [13], is the distance from the focal point at which the intensity decreases by 20 percent.

$$\mathrm{DOF} = \Delta z = \pm \frac{1}{2} \frac{\lambda}{(\mathrm{NA})^2} = \pm \frac{2(\Delta r)^2}{\lambda} \qquad (10)$$

Zone plates have relatively low efficiencies. In these structures, typically only 10 percent of the light is focused by the first diffracted order. 50 percent of the light is absorbed by the opaque zones, 25 percent is transmitted by the 0^{th} order and 10 percent goes to the divergent –1 order. The rest is distributed amongst the higher orders of the zone plate.

2.3 Zone Plate Fabrication.

All the Fresnel zone plates used in this thesis were fabricated at the Center for X-Ray Optics, Lawrence Berkeley National Laboratory (LBNL) using an electron beam lithography tool, the Nanowriter [22-25]. The fabrication process is illustrated in Fig. 2.4. Fabrication begins with a silicon wafer containing: a back-etched window covered with a thin (100 nm thick) silicon nitride layer, an etch resistant 10 nm thick plating base, and a several hundred nanometers thick polymer and electron-sensitive resist layer. A high energy electron beam writes the desired pattern into the resist material. The areas exposed by the electron beam are cryogenically etched away to form a mold structure. This pattern is then electroplated with gold or nickel, which acts as an absorber. The remaining resist and polymer are then stripped, leaving a zone plate of metallic absorbing rings supported by the semi-transparent silicon nitride

membrane.

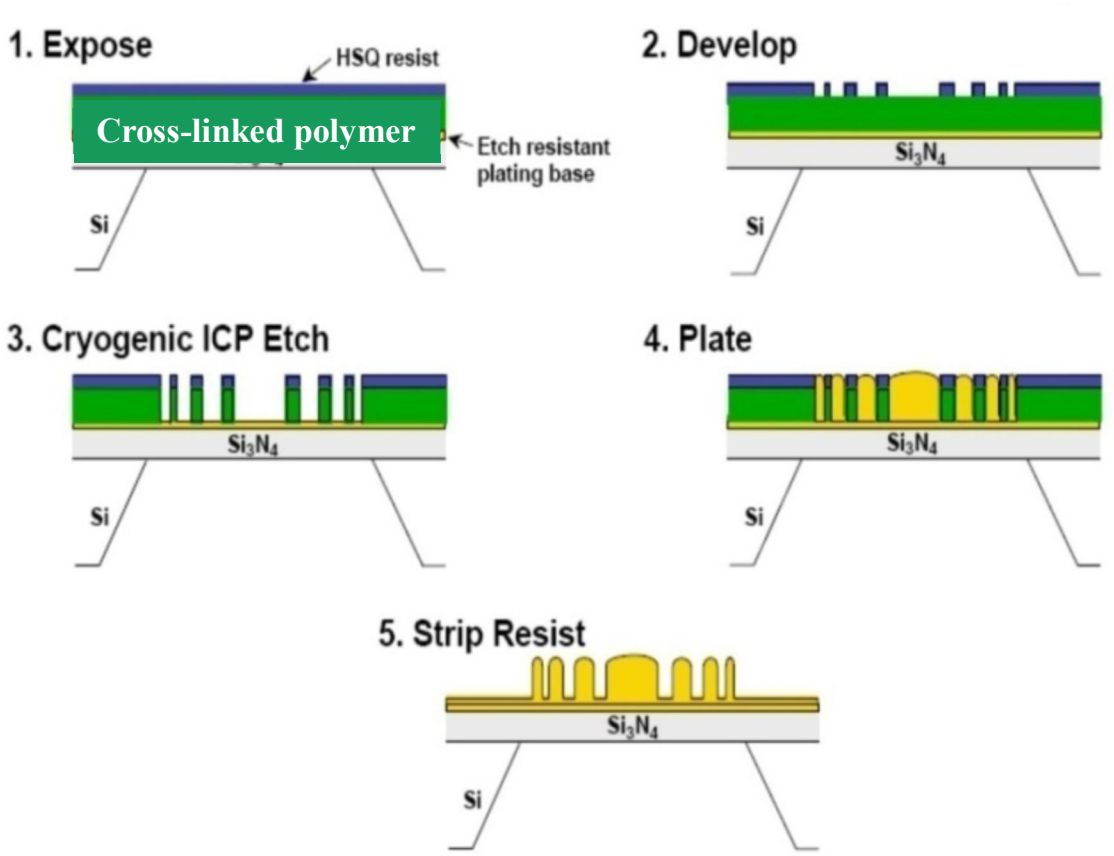

Fig. 2.4 Illustration of steps in the fabrication of zone plate (Figure from [15]) .

In the EUV region corresponding to the wavelength of the Ne-like Ar laser, 46.9 nm, the absorption of the silicon nitride is high, and a structure without a supporting membrane must be used. In such "freestanding zone plate", pseudo-random supports between the opaque zones are used to hold the structure together without significantly compromising the performance of the lens. Figure 2.5 shows SEM images of a zone plate with a silicon nitride substrate and a

freestanding zone plate in which the substrate has been removed.

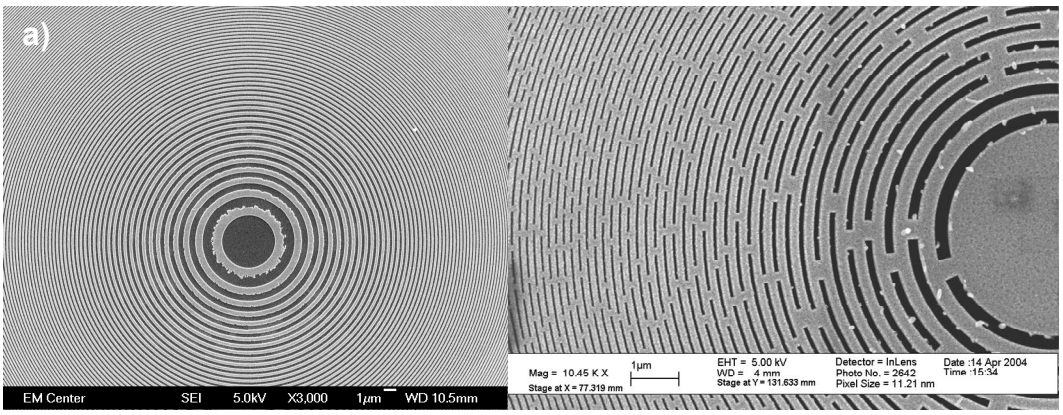

Fig. 2.5 SEM images of (a) a zone plate on a silicon nitride substrate and (b) a freestanding zone plate where the substrate has been removed. The pseudo-random supports are visible (Figure from [15]).

The freestanding design was used to maximize the throughput, as the use of any thin film substrate material would significantly attenuate the 46.9 nm laser light. The zone plate has 10 percent efficiency in the first order focus. The zone plate used in the experiments described below had a diameter of 0.5 mm, an outer zone width of 200 nm, and a NA of 0.12. The focal distance of this lens was 2.13 mm and the depth of focus, 3.41 μm. Table 2.1 summarizes the most important parameters of the zone plate for first and third order.

Table 2.1 Parameters for the 200 nm outer zone-width zone plate with 625 zones and diameter of 0.5 mm.

Parameter	First order	Third order
Numerical aperture	0.12	0.36
Spot size	230 nm	80 nm
Diffraction efficiency	10%	3%
Focal length	2.13 mm	0.71 mm
Depth of focus	3.32 μm	1.08 μm

2.4 EUV-Laser Based Nanometer-Scale Machining Set Up.

Figures 2.6(a) shows an schematic diagram of the experimental set up used to demonstrate nano-scale ablation with a focused EUV laser beam. A photograph of the setup showing the EUV capillary discharge laser and the processing vacuum chamber is displayed in Figure 1b. Ablation is produced using a Fresnel zone plate (FZP) to focus pulses from a compact $\lambda = 46.9$ nm capillary discharge laser onto a Si wafer coated with PMMA. The laser (right of Fig. 2.6b) produces laser pulses by the amplification of spontaneous emission in a dense plasma of eight times ionized argon atoms (Ne-like Ar). For this experiment an alumina capillary discharge tube 27 cm in length and 3.2 mm inner diameter was used to produce 0.1 mJ laser pulses of 1.2 ns duration at a repetition rate of 1-2 Hz.

At 1.2 meter distance from the capillary channel exit, where the FZP is located, the beam significantly overfills the 0.5 mm aperture of the zone plate, and therefore only a small portion of the laser beam energy is incident upon the surface of the focusing optic. The first order efficiency of the zone plate is 10 percent. The third order focus contains only 10 percent of the energy of the first order focus. The fluence onto the sample was further reduced by introducing a selected pressure of argon gas into the processing chamber as a mean of attenuating the beam by photoionization of the argon atoms by the 24.6 eV laser photons.

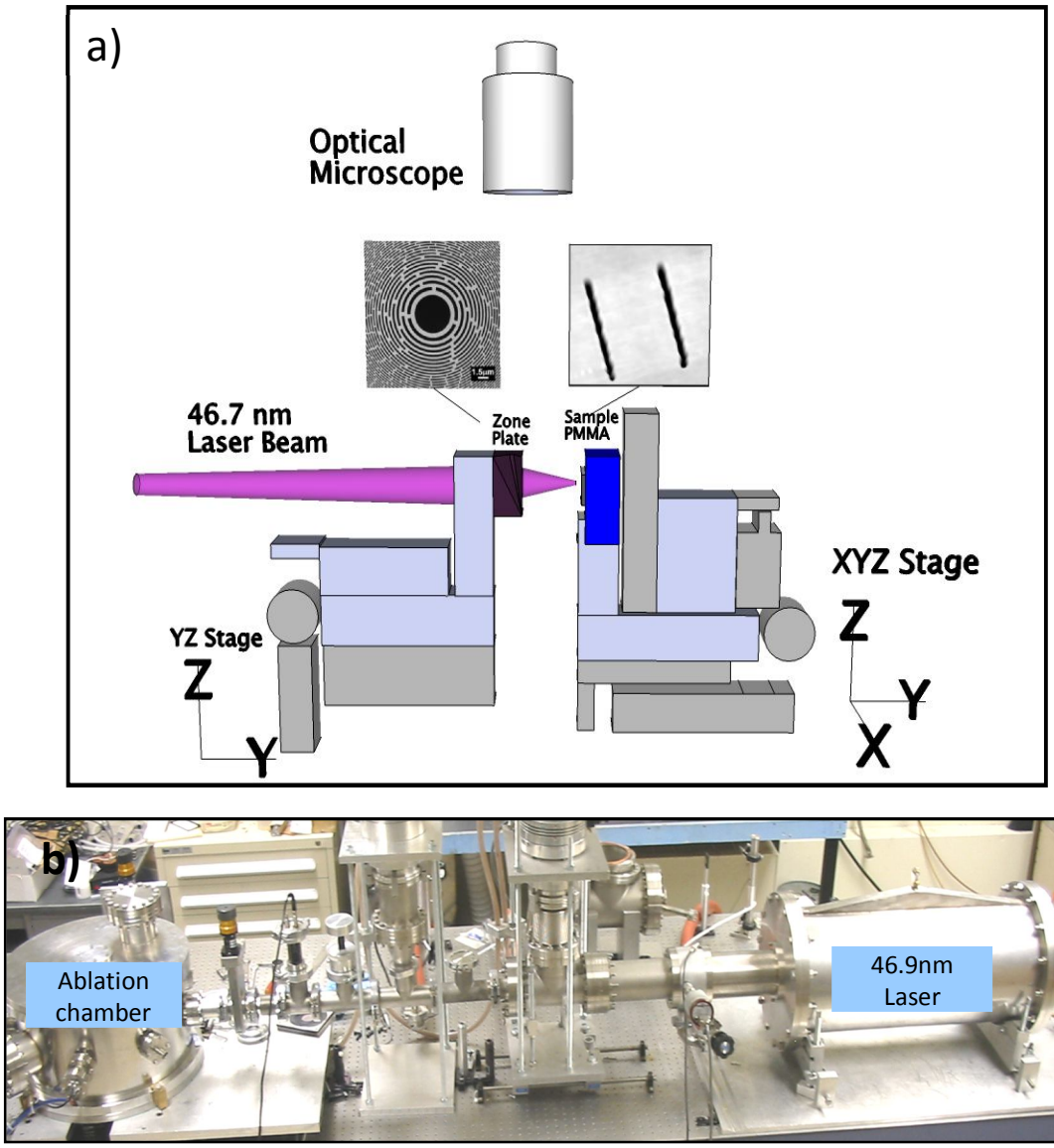

Figure 2.6. (a) Top view schematic representation of the set up used to demonstrate EUV laser nano-machining. The output of a 46.9 nm capillary discharge EUV laser is focused with a Fresnel zone plate lens onto the sample. (b) Photograph of the nanometer-scale machining laser system showing the 46.9nm capillary discharge laser (right) that is attached to the processing chamber (left).

As discussed in Chapter 1, in previous ablation work with focused EUV laser pulses the smallest diameter craters had been obtained placing the sample at 7 μm from the plane of the third order focus [17]. In principle, the spot diameter at that location should be three times smaller than at the first order focus. However, because the zone plate used in the experiments

was corrected for aberrations in the first order focus but not in the third, this was not the case. Nevertheless, it was found that at several micrometers of the location of the third order focus the beam intensity distribution is characterized by a narrow central peak 100 nm in diameter surrounded by several concentric rings of decreasing intensity. Attenuation of the beam intensity in the rings to the point at which the beam did not cause significant material removal allowed the creation of the smallest craters, 82 nm in diameter [17]. A similar procedure was used to produce the trenches reported in this thesis.

The sample was positioned into a kinematic mount which was magnetically attached to an XYZ stage to ensure it is placed back at the same position every time it was removed for inspection. In this configuration, the sample can be displaced ±12.5 mm in the X and Y directions with up to ±1 μm resolution. The surface of the sample was aligned at 90° with respect to the laser beam axis, Z. The displacement in the direction perpendicular to the beam axis was accomplished by means of a closed loop piezoelectric actuator that has a resolution of 50 nm.

The sample consisted of a 90 nm thick layer of PMMA (MicroChem, 950,000 molecular weight) coated onto a silicon wafer. The sample was first pre-positioned at a distance of 2.1 mm from the FZP with the aid of a 10x visible light microscope, a distance that corresponds to the 1st diffraction order focal distance of the 200 nm outer zone width FZP. Trenches were ablated on the PMMA layer by moving the sample along Z with the piezoelectric actuator at a velocity of 50 nm/s while firing the laser at 1or 2 Hz repetition rate. The ablated patterns were analyzed with an atomic force microscope (AFM) used in tapping mode with a 10 nm radius, 30º cone angle cantilever tip (MicroMasch, NSC16).

2.5 Nanometer-Scale Machining Results.

The large ablation craters, shown on the right in Figure 2.7, were obtained without attenuating the laser beam by placing the sample near the 1st order focus of the zone plate.

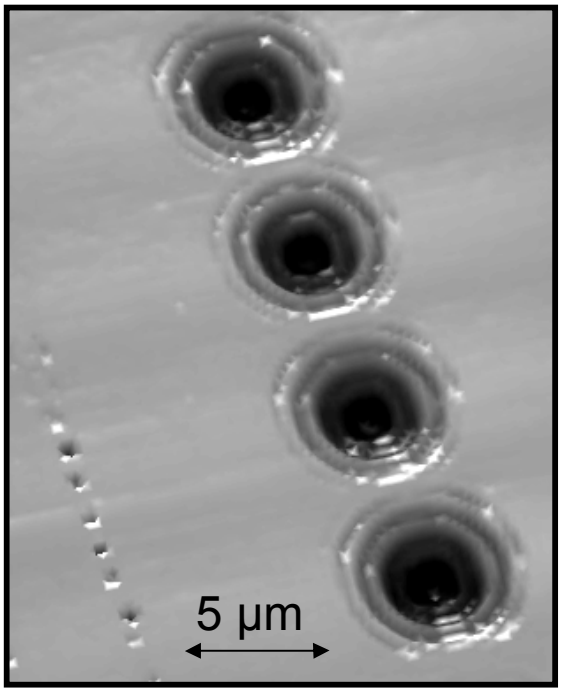

Figure 2.7. AFM image of ablation craters produced by EUV laser ablation in PMMA using the un-attenuated beam with first diffraction order focusing (center right, un-optimized sample position) and third diffraction-order focusing (bottom left corner).

Inspection of the sample with an AFM showed that craters were produced when the sample was positioned as far away as ±25 µm from the calculated focus position. Depending on how close the sample was to the 1st order focal plane, the craters diameter varied between 1 to 5 µm in diameter. Since these un-optimized first diffraction order craters were easily obtained and could be located with a visible light microscope, they were used as a reference to find the smaller

craters that were created positioning the sample near the third diffraction order focus of the zone plate.

Ablation at the 3rd order focus was realized by initially pre-positioning the sample at a distance approximately equal to the 3rd diffraction order focal distance of the 200 nm of the FZP, approximately 0.71 mm. Figure 2.8 shows an AFM image of trenches machined when positioning the sample at different distances from the third order focus of the FZP.

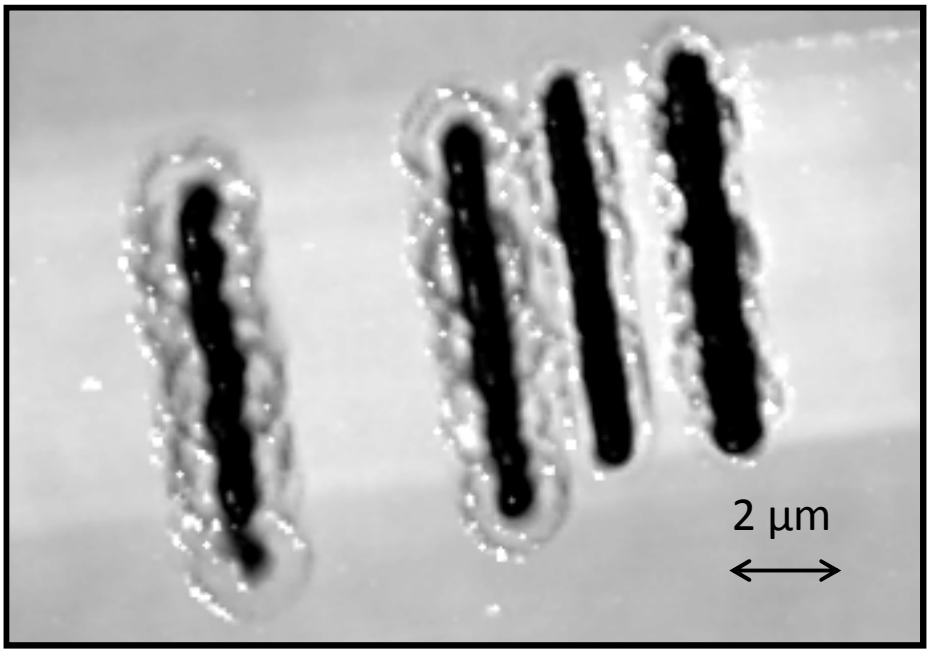

Figure 2.8. Trenches machined on PMMA with the un-attenuated 46.9 nm laser beam by positioning the sample at four different distances near the third-order plane. The left most trench has an average width of 1 µm, and the diameter of the surrounding rings approach 2 µm.

Each trench was ablated after re-positioning the sample at steps of approximately 1 µm. Without attenuation of the EUV laser beam the entire thickness of the PMMA layer was ablated by a single laser shot, with the trenches reaching the surface of the silicon wafer. Without beam attenuation concentric rings are noticeable surrounding the trenches (Fig. 2.8). With sufficient beam attenuation the rings are no longer observed, making it possible to obtain clean narrow

trenches. For this purpose several experimental runs were conducted attenuating the EUV laser beam by introducing argon gas into the path of the laser. Attenuation of the beam results in a reduction of the width and depth of the trenches, and no visible surrounding ablation rings are observed. Figure 2.9 shows trenches ablated attenuating the beam by a factor of 8. As the sample was moved away from the focal plane, the width of the trenches decreases as shown from right to left in Figure 2.9a.

The average widths of the ablated trenches at the surface are 250 nm, 280 nm, and 295 nm. The respective average full widths at half maximum starting from the left most groove are 160 nm, 180 nm and 182 nm. At this level of attenuation the entire thickness of the PMMA layer is still ablated, with the grooves reaching the surface of the silicon wafer as shown in Figure 2.9b.

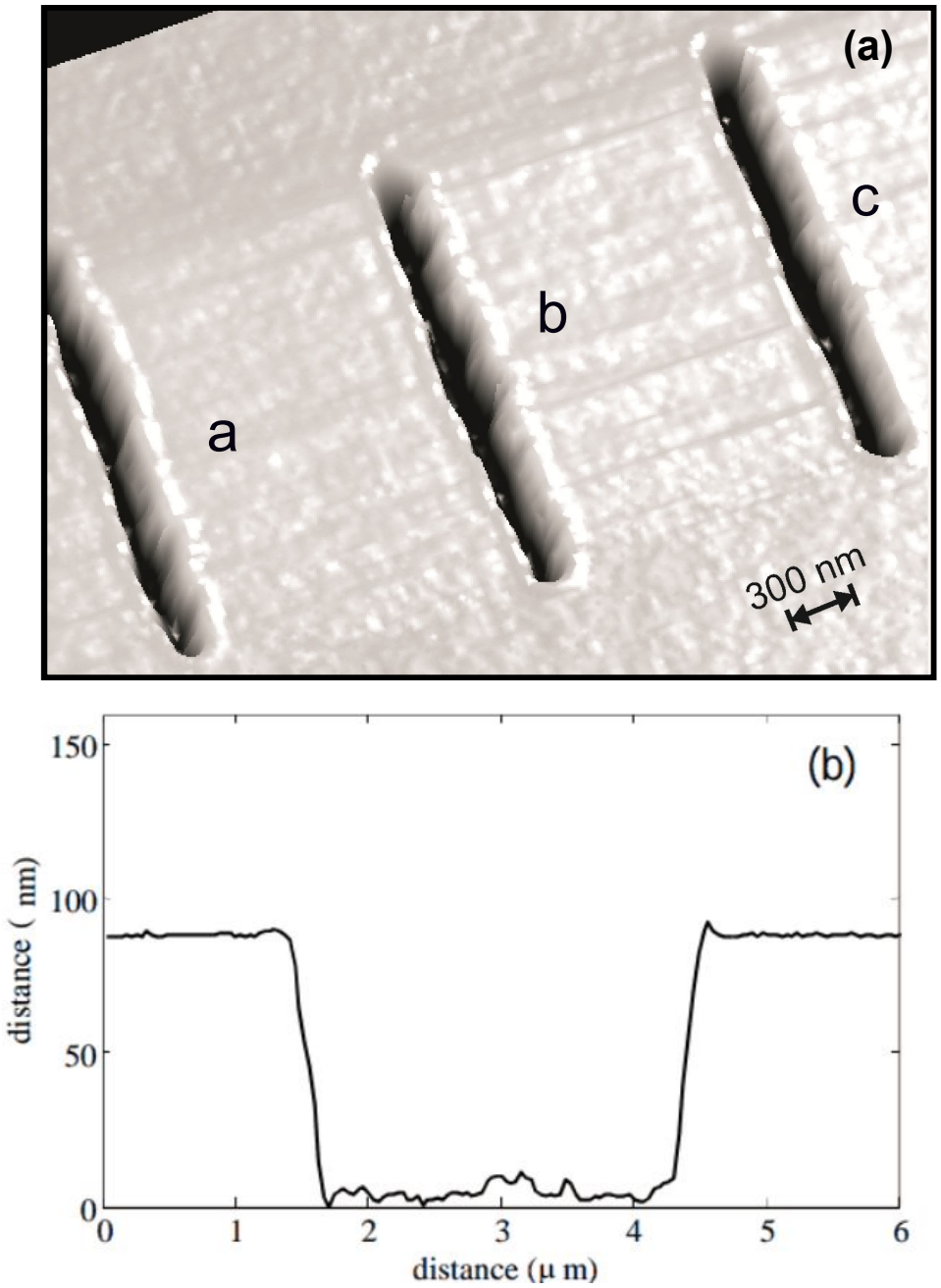

Figure 2.9.(a) Trenches machined on PMMA with a 46.9 nm laser beam positioning the sample at three different distances from the third order focus of the zone plate and attenuating the beam by 8x. The groove on the left has a FWHM of 160 nm and a width at the surface of 250 nm. (b) Cut out of right most trench showing thickness of PMMA ablated away reaching the surface of the silicon wafer.

With an increased attenuation of the laser beam to factor of 16x, trenches with narrower widths were achieved. Figure 2.10 (a) shows a set of trenches ablated under this condition. Figure 2.10 (b) shows a lineout across trenches a, b and c.

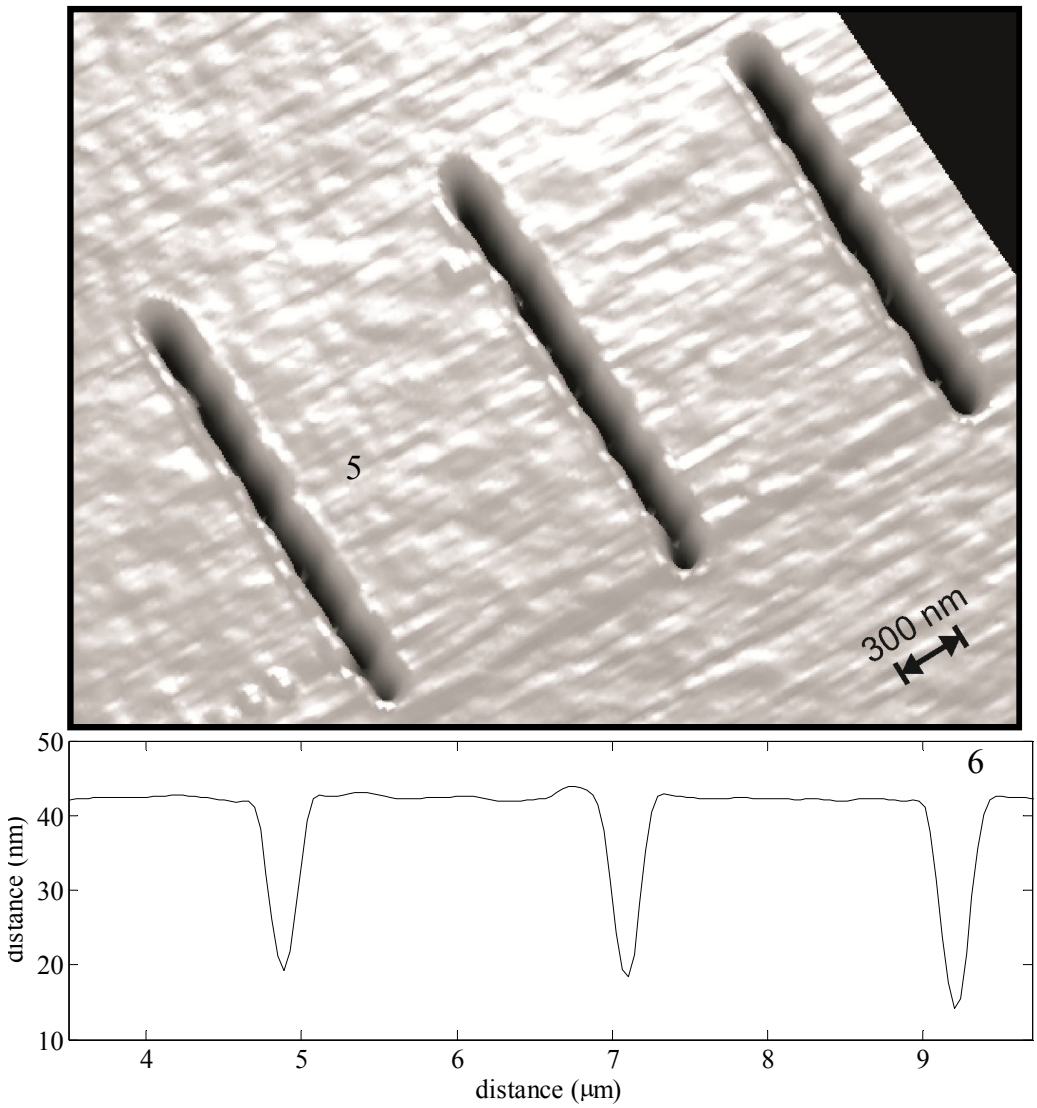

Figure.2.10 (a) Trenches machined on PMMA with a 46.9 nm laser beam by positioning the sample at three different distances from the third order focus of the zone plate attenuating the beam by 16x. The groove on the left has a FWHM of 130 nm and a width at the surface of 200 nm. (b) Lineout across trenches a, b, and c.

The average widths at the surface of PMMA, starting from the left most groove are 200 nm, 250 nm, and 270 nm. The corresponding FWHM are 130 nm, 135 nm and 145 nm. The trenches are observed to have cleanly cut walls and sharp edges that are not affected by thermal damage. This is a result of the strong localization of the absorbed energy. Both the absorption length of the 46.9 nm light and the thermal diffusion (19 nm) and thermal diffusion lengths (10 nm) are short. The observed line edge roughness along the grooves is the result of shot-to-shot variation of the laser pulse energy with a possible contribution from laser beam pointing instabilities. The depth of the trenches, shown in Figure 2.10(b), is observed to increase from 22 to 30 nm as the sample plane moves closer to the calculated focus.

In a first step towards machining metals, insulators, and semiconductors our group has recently used a similar set up to ablate small holes in thin films of gold and hafnium oxide, and in silicon wafers. The results demonstrate for the first time the feasibility of directly machining of nanometer-scale features with a focused EUV laser beam. Parameter optimization is likely to result in the direct patterning of sub-100 nm features. The recent demonstration of high repetition rate table-top lasers that generate picosecond pulses with energies up to 10 μJ in the 13 nm spectral region [19] should further reduce the minimum achievable feature size.

CHAPTER 3: STUDY OF EUV LASER-CREATED PLASMAS.

3.1. Introduction

This chapter discusses the physics of the interaction of the focused EUV laser beam with a solid surface. The ablation process is closely related to the characteristics of the plasma that is created. The fundamentally different mechanisms by which intense EUV light interacts with materials defines a regime of laser– plasma interaction that differs significantly from that corresponding to plasmas created by optical lasers. The fact that EUV wavelengths are associated with critical densities that exceed solid density (e.g., $n_c = 5 \times 10^{23}$ cm $^{-3}$ for λ=46.9 nm light) results in greatly decreased Bremsstralung absorption and in the direct deposition of a large fraction of the laser pulse energy in the solid target, in which the initial depth of the heated region is determined mainly by the absorption coefficient of the material. The high photon energy of EUV beams exceeds the ionization energy of all neutral atoms and low-charge ions present, resulting in direct single-photon ionization of the plasma, an absorption mechanism unavailable to optical lasers. These fundamental disparities result in different energy deposition mechanisms and consequently in different plasma characteristics and dynamics. By using short EUV laser pulses, plasmas with very uniform conditions can be created over relatively large volumes [26].

The availability of high-intensity EUV lasers creates the opportunity to study the unique properties of plasmas created by intense monochromatic EUV light. Moreover, since EUV laser beams can be focused into spots less than 100 nm in diameter [17], the study of plasmas created by focused EUV lasers is of practical interest for the development of a new generation of nanometer-scale probes with analytic capabilities. Tabletop EUV laser beams generated by collisional electron impact excitation of ions in discharge-created and laser created plasmas can

be focused to generate plasmas with pulses ranging from the nanosecond [28] to the picosecond time scales. The advent of EUV free electron lasers [12] will allow the study of plasmas heated by extremely intense EUV pulses in the complementary femtosecond time scale. In anticipation to experiments, theoretical studies have been conducted that predict that the characteristics of plasmas created with intense monochromatic EUV light will depend strongly on the target material and differ significantly from those created with visible lasers [17]. However, to our knowledge no experimental results of the study of the characteristics of such plasmas have been reported. A few groups have investigated the ablation of materials with focused EUV laser beams [12,27-28,37-38], but the studies concentrated on the effects on the ablated targets and not on the plasma phenomena.

This section reports the spectroscopic study of plasmas created by focused EUV laser pulses of 1 ns duration on solid targets and compares the results with hydrodynamic–atomic physics model simulations. Low temperature plasmas were generated by irradiating low- Z (Si), and mid-Z (Cr and Ag) slab targets with the focused beam from a 46.9 nm wavelength (26.5 eV) Ne-like Ar capillary discharge EUV laser. The measurements show, in accordance with hydrodynamic model calculations, that the much lower absorption coefficient for Si at this wavelength results in plasmas that are significantly colder and less ionized than Cr and Ag plasmas, in spite of the faster expansion of the Cr and Ag plasmas. The nanosecond regime of EUV laser pulses investigated here differs and is complementary to the studies that will be conducted at the EUV free electron laser, which will employ pulses in the femtosecond time scale. In the nanosecond regime thermal heat conduction and expansion of the plasma into vacuum play a significant role. Thermal conduction can increase the amount of ablated material, and expansion causes significant hydrodynamic cooling.

3. 2 Experimental Set Up.

A schematic diagram of the experimental setup is shown in Fig. 3.1. Si, Cr, and Ag targets were irradiated by the beam of a 46.9 nm Ne-like Ar capillary discharge EUV laser focused with a 10 cm radius of curvature spherical mirror. The laser pulses are produced by collisional electron impact excitation of Ne-like ions in a plasma column generated by a fast capillary discharge [41,42]. The plasma column is generated by injecting a 24 kA peak amplitude current pulse through a 3.2 mm diameter alumina tube filled with 410 mTorr of Ar gas. In the configuration used in this experiment the laser produces pulses of 100μJ energy and 1.2 ns duration. The experiments were conducted in a vacuum chamber placed at 130 cm from the output of the laser. The laser beam was focused onto the target by using a mirror coated with Sc/Si multilayers [43], producing a focal spot of 10–15 μm diameter. The targets consisted of thin slabs that intersect part of the incoming laser beam (Fig. 3.1), reducing the irradiation fluence on target and making the focal spot slightly asymmetric. Shots with reduced irradiation energy were obtained by attenuating the beam with 0.2 μm thick, freestanding Al foils with measured transmissivity of 17 percent at 46.9 nm. The targets were placed on a motorized translation stage that allowed the selection of the irradiated area and distance to the focusing mirror.

Light emitted by the plasma was collected by a 10 cm focal length fused silica lens to create a 1-to-1 image of the plasma onto the entrance slit of a 0.3 m focal length visible–ultraviolet spectrometer. The dispersed light was detected by using a back-illuminated CCD detector array. The light collection system was sufficiently efficient to produce line spectra from

a single laser shot. However, most spectra were obtained by accumulating several laser shots to improve the signal-to-noise ratio.

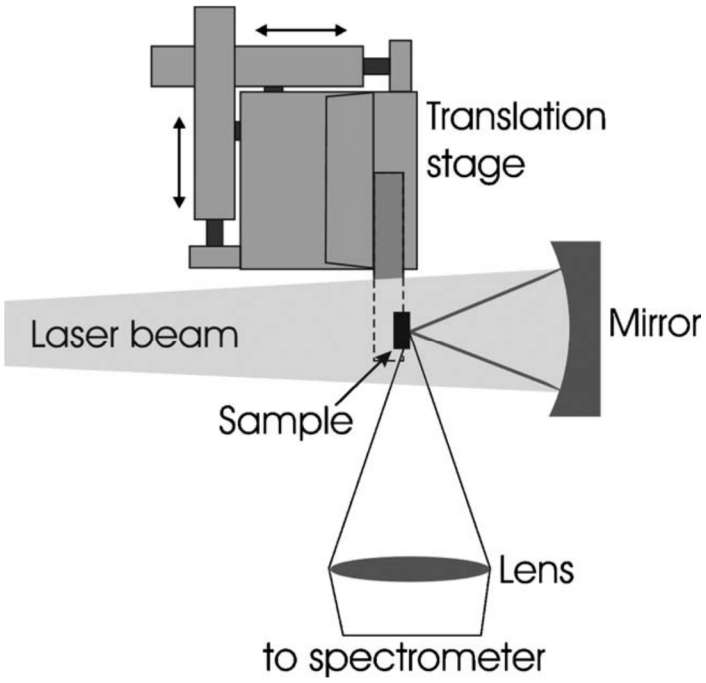

Fig. 3.1. Experimental setup used for the generation and spectroscopy of EUV laser-created plasma. The vacuum chamber is not shown.

Similar experiments were performed by irradiating the samples with 120 ps optical laser pulses (λ=800 nm) produced by a Ti:sapphire laser system consisting of a mode-locked oscillator, a grating stretcher, and a multipass amplifier. In this case the laser beam was focused into a 35 μm diameter spot by a 15 cm focal length fused silica lens. Spectra of the resulting plasmas were recorded by using the same setup.

3.3 Experiment and Simulation Results.

Experiments were conducted by irradiating the targets with three different EUV laser pulse energies, 0.5, 3.1, and 17 μJ, corresponding to peak intensities of 4 $x10^8$, 2.5$x10^9$, and 1.4$x10^{10}$ W/cm^2, respectively. The plasmas were modeled with a 1 1/2-dimension hydrodynamic-atomic code [44]. The hydrodynamic equations were solved in 1D, with the lateral expansion taken into account using the self-similar solution for expansion into a vacuum [45]. The 1 1/2-dimensional code includes a collisional–radiative atomic model with multicell radiation transport, which solves for the ground state and excited populations by using a quasi-steady-state solution. Both inverse Bremsstrahlung absorption as well as photoionization are included as energy deposition mechanisms for the EUV laser. Photoionization absorption is calculated by using the ion distribution from the atomic model, with the photoionization cross section for each ion. The atomic data is obtained from the Flexible Atomic Code (FAC) [45] with photoionization cross sections from Reilman and Manson [46]. A postprocessor was used to synthesize spectra based on multicell radiation transport and the computed populations and opacities. To improve the accuracy of the synthesized spectra the level energies and transition probabilities were calibrated by using experimental data when available [47].

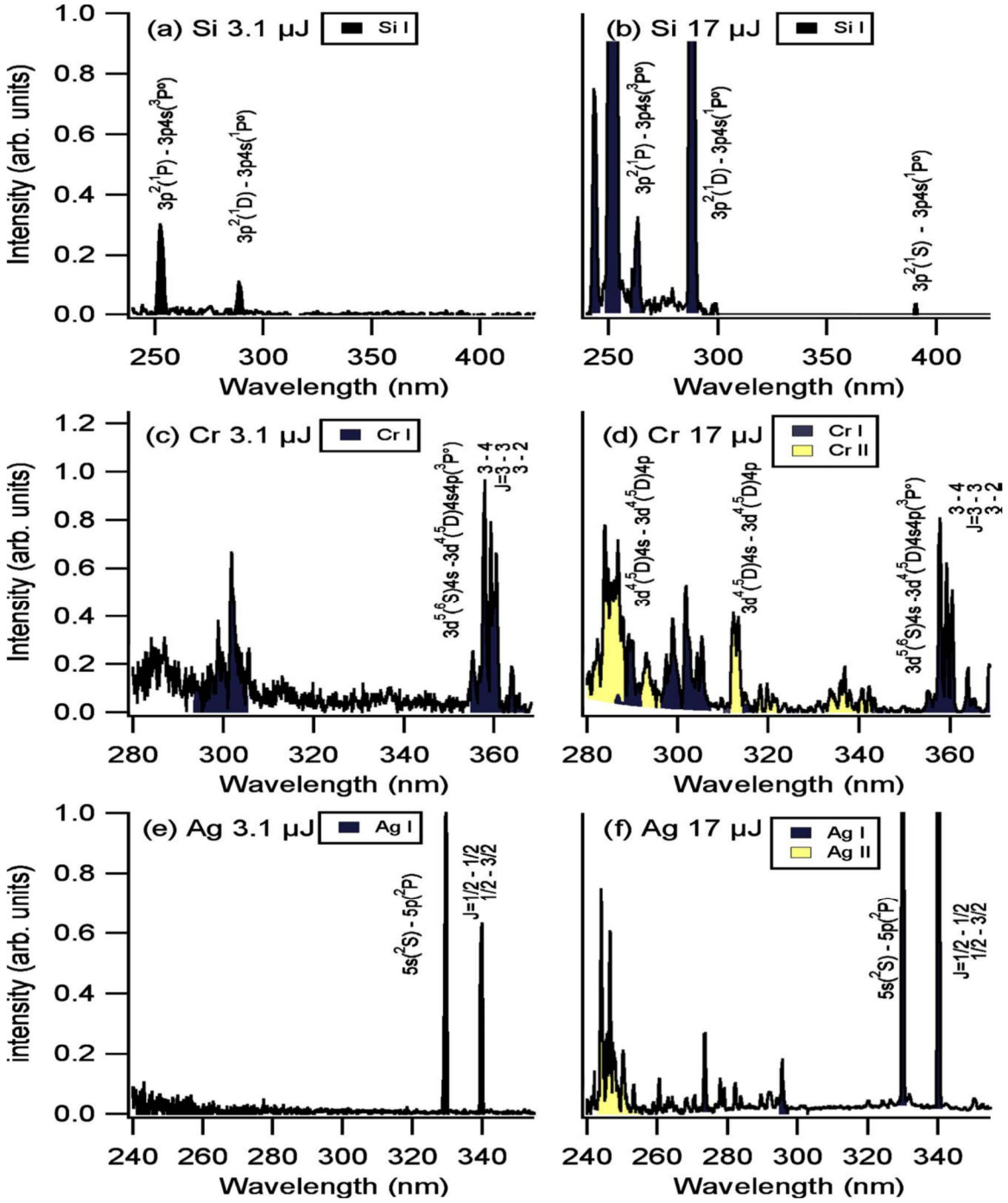

Fig.3.2. Experimental spectra of Si, Cr, and Ag plasmas obtained by irradiating solid targets with 3.1 and 17μJ, 46.9 nm EUV laser pulses. At 3.1μJ (a) Si is only slightly above the ablation threshold, while for both (c) Cr and (e) Ag strong lines from neutral atoms are present. At 17μJ only neutral atom lines are present for (b) Si, while the (d) Cr and (f) Ag spectra show lines from both the neutral atoms and the singly charged ions.

At the lowest irradiation energy investigated, 0.5μJ, all three elements were found to be below the ablation threshold, in agreement with the simulations. At the intermediate energy of 3.1 μJ plasma radiation from neutral Cr and Ag atoms was observed (Figs. 3.2c and 3.2e). At this energy Si is very close to the ablation threshold, resulting in only very weak emission from two of strongest Si I lines in the ultraviolet spectra (Fig. 3.2a).

These observations agree with model simulations that predict that the Cr and Ag plasmas reach a peak temperature of 2.2 and 2.8 eV and a peak degree of ionization of $Z=0.5$ and $Z=1.0$, respectively while Si, which is at the threshold of ablation, only reaches a peak temperature of 0.2 eV and a degree of ionization $Z<0.01$. The different behavior of these materials is to be expected, as the absorption length of the 46.9 nm laser light in Si (300 nm) greatly exceeds that of Cr and Ag (18 and 7.5 nm, respectively). Consequently, in Si the EUV light interacts with a much larger volume of material, which results in a higher ablation threshold and in a colder plasma.

At the highest irradiation energy (17 μJ) plasma radiation was observed for all three elements. Figure 3.2 shows the measured time-integrated visible spectra corresponding to Si (Fig. 3.2b), Cr (Fig. 3.2d), and Ag (Fig. 3.2f) plasmas for this irradiation condition. The Si spectra of Fig. 3.2(b) still displays only lines associated with neutral Si (Si I). Classified lines from singly charged silicon (Si II) that fall within the spectral window of the measurement (e.g., 207.27, 290.43, and 290.57 nm) are not observed, an indication that this is a very low-temperature plasma, in agreement with model calculations. In contrast, spectra of plasmas

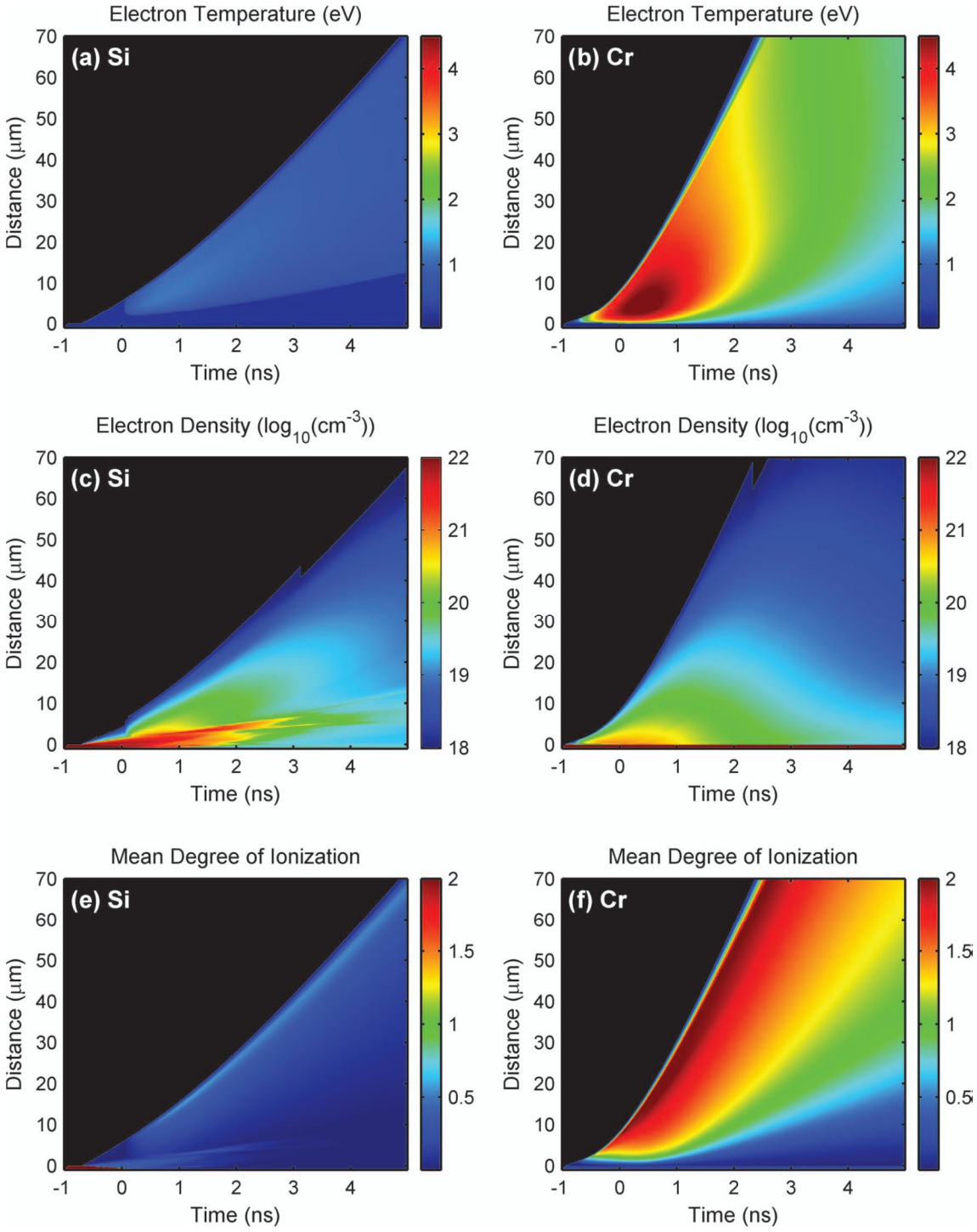

Fig. 3.3 Computed plasma parameters corresponding to Si and Cr plasmas generated by 17μJ energy, 1.2 ns duration EUV laser pulse irradiation (λ=46.9 nm) of solid targets. Because of the smaller absorption cross section (a) the Si plasma is significantly colder than (b) the Cr plasma. (d) The Cr plasma expands at a higher rate. Due to the lower temperature (e) the Si plasma has a much lower degree of ionization than (f) the Cr plasma.

created by irradiation of Cr and Ag targets with the same EUV laser intensity show lines of Cr II and Ag II (Figs. 3.2d and 3.2f). Figure 3.3 shows the computed plasma parameters for Si and Cr plasmas created under these irradiation conditions. The peak temperature for Si is 1.1 eV (Fig. 3.3a), while the Cr reaches a significantly higher temperature of 4.5 eV (Fig. 3.3b). This again reflects the difference in the photoionization cross sections at 46.9 nm: 6.1×10^{-19} cm^2 and 5×10^{-18} cm^2 for Si and Cr, respectively.

This difference in the cross-section results in more energy being absorbed by fewer atoms for Cr than for Si. The larger Cr plasma temperature results in a computed peak degree of ionization of 1.6 for Cr as compared with a degree of ionization of only 0.25 for Si (Figs. 3.3f and 3.3e, respectively). Owing to the higher temperature, the Cr plasma has an increased expansion velocity (Figs. 3.3c and 3.3d), which results in significantly denser plasma away from the target surface.

Figure 3.4 shows simulated spectra for Si and Cr for the irradiation conditions corresponding to the experimental spectra of Figs. 3.2(b) and 3.2(d). The computed Si spectra resembles well that observed in the experiments, showing only Si I lines. The synthesized Cr spectrum also reproduces most of the features of the experimental data, but shows a slightly larger ratio between Cr II and Cr I lines and the presence of weak Cr III lines. This is in part because the synthetic spectra are calculated for the plasma conditions on axis of the irradiated spot, where the plasma has the highest temperature. A 2D plasma model would be necessary to further improve the agreement between the computed and the measured spectra. However, some of the differences are due to an incomplete assignment of the energy levels, while others can arise from the bundling of lines in the calculations. The latter is required for computation efficiency, because there are 1350 levels of interest in the neutral and first ion of Cr, emitting

over 100,000 lines. Nevertheless, the computed and measured spectra agree, clearly showing the signatures of significantly less ionized, colder Si plasma.

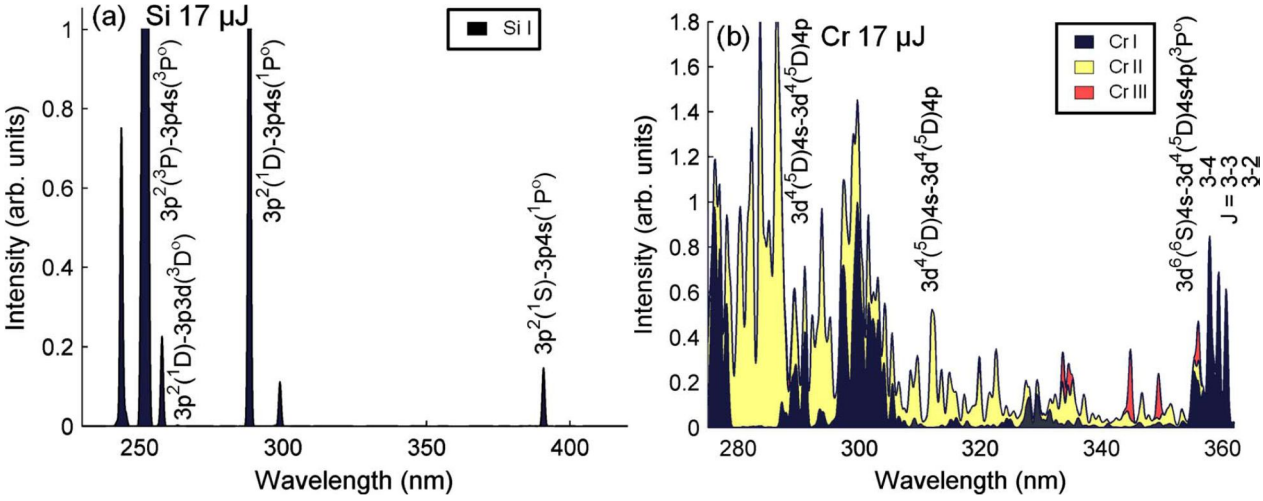

Fig. 3.4. Simulated spectra for Si and Cr plasmas created by 17µJ EUV laser (λ=46.9 nm) pulse irradiation. (a) Si spectrum is completely dominated by neutral atom lines (Si I) (a), while (b) the hotter Cr spectra contains large numbers of both Cr I and Cr II lines.

This behavior of the EUV laser-created plasmas is in contrast to that of plasmas created by irradiation with visible wavelengths, which do not show such strong elemental dependence. In plasmas created with a visible-light laser, once the ablation threshold has been reached, most of the heating occurs via inverse Bremsstrahlung absorption in the plasma near the critical density (1.7×10^{21} cm^{-3} for 800 nm), which is independent of the elemental composition of the target. To verify this different behavior Ti:sapphire laser pulse energies of 97µJ (a few times above the ablation threshold of 25µJ) and 170µJ were used to irradiate Si and Cr samples (Fig. 3.5). At 97µJ, Si I, Si II, and weak Si III lines are observed in the silicon spectra, and Cr I and Cr II lines in the Cr spectra. For 170µJ, strong Si I, Si II, and Si III lines are present, while the ratio of Cr II to Cr I lines increases slightly. The spectra indicate that the degree of ionization for both elements is similar, in sharp contrast to the case of irradiation with EUV light, where for all

laser energies Si is observed to be less ionized than Cr because of the significant differences in the photoionization cross section. In addition to the elemental dependence the EUV laser plasmas can be expected to exhibit strong wavelength dependence [25], governed by the relative position of the laser wavelength respect to the absorption edges of the material.

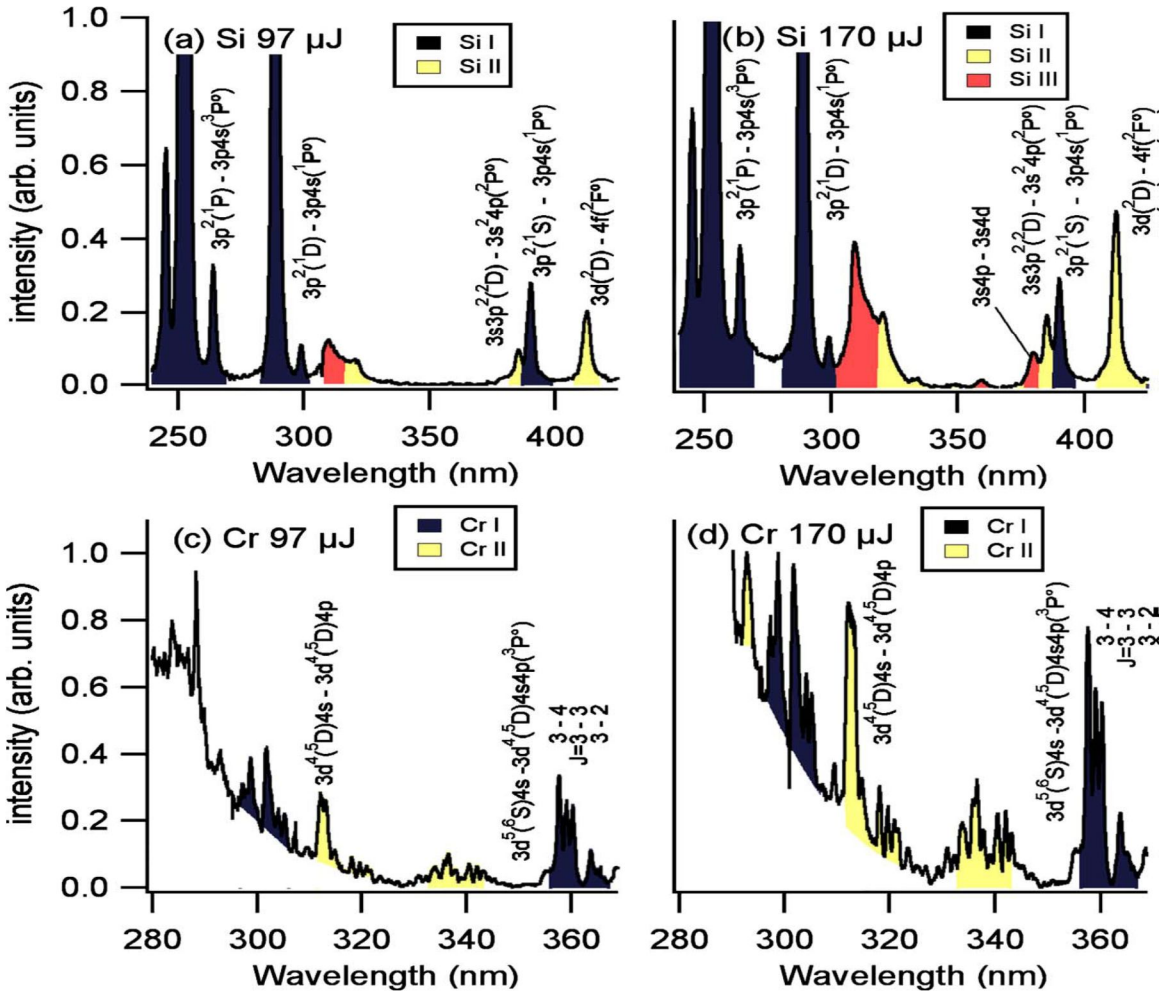

Fig. 3.5. Spectra of (a), (b) Si and (c), (d) Cr created by λ =800 nm laser pulses of 120 ps duration. Si II, Si III, and Cr II lines are emitted from the plasmas created by the 90 and 170μJ pulses.

Simulations were also conducted for higher irradiation energies. The results show that as the intensity of the EUV laser is increased, the behavior of the different elements tends to converge. When the laser energy is increased by a factor of 10, the temperature of the Si plasma

is computed to increase slightly above 3.5 eV, while that of the Cr and Ag plasmas increases to 9.0 and 6.5 eV respectively. Additionally, the mean degree of ionization increases to Z=1.4 for Si and to 2.5 and 2.7 for both Cr and Ag. If the laser energy is further increased by a factor of 100, to 1.7 mJ, the electron temperature is computed to reach 7 eV for Si, 16 eV for Cr, and 10 eV for Ag, while the degree of ionization of the Si plasma, Z=2.5, is calculated to approach that for Cr and Ag, Z=3.0 and Z =3.2. The predicted convergence of the plasma parameters as the irradiation flux is increased is caused by the fact that the amount of mass ablated from the three materials tends to equalize at increased irradiation. This is caused by the more rapid increase in the degree of ionization for Cr and Ag that causes these plasmas to become more rapidly transparent than Si to the 25 eV laser photons (depleted of the absorbing neutral and singly charged ions). At high irradiation energies plasmas with a very uniform degree of ionization can be created. For example, the degree of ionization of a Ag plasma created under the high-intensity condition (1 ns after the peak of a 1.7 mJ laser pulse) is computed to vary by less than 10 percent over 90 percent of the entire plasma volume. However, the plasma density within the volume changes significantly owing to expansion. The degree of ionization of which the plasma becomes transparent increases as the laser wavelength decreases. Therefore shorter-wavelength EUV lasers will create hotter plasmas and preserve the differences between elements until the plasma reaches a higher degree of ionization.

The behavior of the plasmas that will be generated by femtosecond EUV laser pulses will maintain the strong elemental dependence, but important differences exist. Because of the short pulse duration thermal conduction and expansion do not play a significant role. For the nanosecond-duration EUV laser pulses used in our experiment the ablation depth can be significantly deeper than the penetration of the EUV light owing to thermal conduction into the

solid target during and after pulse irradiation. For example, at 17μJ the ablation depth of Si is 1000 nm, corresponding to 3× its absorption length (320 nm), while for Cr the ablation depth is 100 nm, which is 8× the absorption length (13 nm). By contrast, for femtosecond pulses thermal conduction is insignificant during the pulse, yielding ablation depths that more closely match the absorption length. Additionally, expansion of the plasma during the laser pulse is dramatically reduced for a femtosecond pulse. As a result, the plasma density is much more uniform than for the 1ns pulses studied. This will allow the generation of large plasma volumes with nearly constant temperature, density, and degree of ionization.

CHAPTER 4: CONCLUSION AND FUTURE WORK.

We have constructed an ablation test bed based on a compact 46.9 nm EUV laser and have demonstrated the feasibility of performing nanometer-scale machining on PMMA with a focused EUV laser beam. Clean trenches having a top width of 200 nm and a FWHM of 130 nm and several micrometers in length were machined. These are, to our knowledge, the smallest ablated trenches machined on PMMA to date. These results demonstrate the feasibility of performing nanometer-scale machining with focused EUV laser beams. Trenches with narrower widths could be achieved by improving the laser output pointing stability and shot-to-shot pulse energy variations.

We have also studied warm plasmas generated by focusing 46.9 nm EUV laser pulses of nanosecond duration onto Si, Cr, and Ag solid targets. The critical density corresponding to this wavelength (5×10^{23} cm^{-3}) exceeds the solid density, and absorption is dominated by single photon photoionization. Spectra of the EUV laser-created plasmas were compared with those of plasmas created with an optical laser (λ=800 nm). The results agree with hydrodynamic model in showing that the EUV laser plasmas differ from those created by visible lasers and are strongly element dependent, with characteristics largely determined by the position of the laser wavelength relative to absorption edges and resonances. Measured spectra agree with model simulations in showing that EUV laser created Si plasmas, a comparatively low-absorption material at 46.9 nm, are significantly colder and less ionized than plasmas created from more highly absorbent materials such as Cr and Ag. This strong elemental dependence is computed to soften at high nanosecond pulse irradiation intensities that deplete the low-charge species, whose photoionization cross sections dominate the plasma absorption. High-intensity EUV lasers

generating shorter pulses will be able to create highly uniform warm dense plasma over large volumes.

REFERENCES.

[1] X.Liu, D.Du, and G. Mourou. *Laser Ablation and Micromachining with Ultrashort Laser Pulses.* IEEE Journal of Quantum Electronics, Vol.33, No.10, October 1997

[2] F. Korte, J. Serbin, J. Koch, A. Egbert, C.Fallnich, A. Ostendorf, B.N. Chichkov. *Towards nanostructuring with femtosecond laser pulse.* Appl. Phys. A 77, 229-235 (2003)

[3] A. Borowiec, H. K. Haugen. *Femtosecond laser micromachining of grooves in indium phosphide.* Appl. Phys. A 79, 521-529 (2004)

[4] Clark- MXR, Inc., MI

[5] M. Jackson, and G. M. Robinson. *Microfabrication and Nanomanufacturing.* CRC Press, Boca Ranton, Florida 2006.

[6] S. Nolte, B. N. Chichkov and H. Welling. Y. Shani, K. Lieberman, and H. Terkel. *Nanostructuring with spatially localized femtosecond laser pulses.* Optics Letters / Vol. 24, No. 13/ July 1, 1999.

[7] Y.Lin, M.H.Hong, W.J.Wang, Y.Z.Law, T.C.Chong. *Sub-30 nm lithography with near-field scanning optical microscope combined with femtosecond laser.* Appl.Phys.A80,461–465(2005) withdrawal

[8] Ivan Avrutsky, Daniel G. Georgiev, Dmitry Frankstein, and Gregory Auner. *Super-resolution in laser annealing and ablation.* Applied Physics Letters. Volume 84, Number 13 (2004).

[9] P.E. Dyer. *Excimer laser polymer ablation: twenty years on.* Department of Physics, University of Hull, Hull, HU67RX, UK. Appl. Phys. A77,167–173(2003)

[10] P.Simon, J.Ihlemann. *Ablation of submicron structures on metals and semiconductors by femtosecond UV-laser pulses*. Applied Surface Science 109r110199725–29

[12] W. Ackermann, G. Asova, V. Ayvazyan, A. Azima, N. Baboi, J. Bähr, V. Balandin, B. Beutner, A. Brandt, A. Bolzmann, R. Brinkmann, O. I. Brovko, M. Castellano, P. Castro, L. Catani, E. Chiadroni, S. Choroba, A. Cianchi, J. T. Costello, D. Cubaynes, J. Dardis, W. Decking, H. Delsim-Hashemi, A. Delserieys, G. Di Pirro, M. Dohlus, S. Düsterer, A. Eckhardt, H. T. Edwards, B. Faatz, J. Feldhaus, K. Flöttmann, J. Frisch, L. Fröhlich, T. Garvey, U. Gensch, Ch. Gerth, M. Görler, N. Golubeva, H.-J. Grabosch, M. Grecki, O. Grimm, K. Hacker, U. Hahn, J. H. Han, K. Honkavaara, T. Hott, M. Hüning, Y. Ivanisenko, E. Jaeschke, W. Jalmuzna, T. Jezynski, R. Kammering, V. Katalev, K. Kavanagh, E. T. Kennedy, S. Khodyachykh, K. Klose, V. Kocharyan, M. Körfer, M. Kollewe, W. Koprek, S. Korepanov, D. Kostin, M. Krassilnikov, G. Kube, M. Kuhlmann, C. L. S. Lewis, L. Lilje, T. Limberg, D. Lipka, F. Löhl, H. Luna, M. Luong, M. Martins, M. Meyer, P. Michelato, V. Miltchev, W. D. Möller, L. Monaco, W. F. O. Müller, O. Napieralski, O. Napoly, P. Nicolosi, D. Nölle, T. Nuñez, A. Oppelt, C. Pagani, R. Paparella, N. Pchalek, J. Pedregosa-Gutierrez, B. Petersen, B. Petrosyan, G. Petrosyan, L.

Petrosyan, J. Pflüger, E. Plönjes, L. Poletto, K. Pozniak, E. Prat, D. Proch, P. Pucyk, P. Radcliffe, H. Redlin, K. Rehlich, M. Richter, M. Roehrs, J. Roensch, R. Romaniuk, M. Ross, J. Rossbach, V. Rybnikov, M. Sachwitz, E. L. Saldin, W. Sandner, H. Schlarb, B. Schmidt, M. Schmitz, P. Schmüser, J. R. Schneider, E. A. Schneidmiller, S. Schnepp, S. Schreiber, M. Seidel, D. Sertore, A. V Shabunov, C. Simon, S. Simrock, E. Sombrowski, A. A. Sorokin, P. Spanknebel, R. Spesyvtsev, L. Staykov, B. Steffen, F. Stephan, F. Stulle, H. Thom, K. Tiedtke, M. Tischer, S. Toleikis, R. Treusch, D. Trines, I. Tsakov, E. Vogel, T. Weiland, H. Weise, M. Wellhöfer, M. Wendt, I. Will, A. Winter, K. Wittenburg, W. Wurth, P. Yeates, M. V Yurkov, I. Zagorodnov, and K. Zapfe. *Operation of a free- electron laser from the extreme ultraviolet to the water window.* Nat. Photonics 1, 336–342 (2007).

[13] L. Juha, J. Krasa, A. Prag, A. Cejnarova, D. Chvostova, K. Rohlena, K. Jungwirth. J. Kravarik, P. Kubes, Yu. Bakshaev, A. S. Chernenko, V.D. Korolev and V.I. Tumanov, M. I. Ivanov, A. Bernardinello, J. Ullschmied, and F.P. Boody. *Ablation of poly(methyl methacrylate) by a single pulse of soft x-rays emitted from Z-pinch and laser produced plasmas.* Surface Review and Letters, Vol. 9, No.1 (2002) 347-352

[14] Jerzy B. Pełka ,Andrzej Andrejczuk, HenrykReniewicz, Norbert Schell, Jacek Krzywinski, Ryszard Sobierajski ,Andrzej Wawro, Zbigniew R. Zytkiewicz Dorota Klinger, Libor Juha. *Structure modifications in silicon irradiated by ultra-short pulses of XUV free electron laser.* Journal of Alloys and Compounds 382(2004)264–270

[15] Attwood, D.T. *Soft x-ray and extreme ultraviolet radiation: principles and applications*. ed. C.U. Press. 2000.

[16] S. Heinbuch, M. Grisham, D. Martz, and J.J. Rocca. *Demonstration of a desk-top size high repetition rate soft x-ray laser.* Optics Express **13**, 4050, (2005).

[17] Vaschenko, A. Garcia,* C. S. Menoni, and J. J. Rocca, . Hemberg and S. Bloom, W. Chao, E. H. Anderson, and D. T. Attwood, Y. Lu and B. Parkinson . Nanometer-scale ablation with a table-top soft x-ray laser. OPTICS LETTERS Vol.31, No.24

[18] J.J. Rocca, V. Shlyaptsev, F.G. Tomasel, O. D. Cortazar, D. Hartshorn, and J.L.A. Chilla. *Demonstration of a Discharge Pumped Table-Top Soft-X-Ray Laser.* Physical Review Letters. VOLUME 73, NUMBER 16

[19] Benware, B.R., *et al.*, *Demonstration of a high average power tabletop soft X-ray laser.* Physical Review Letters, 1998. **81**(26): p. 5804-5807.

[20] Benware, B.R., *et al.*, *Operation and output pulse characteristics of an extremely compact capillary-discharge tabletop soft-x-ray laser.* Optics Letters, 1997. **22**(11): p. 796-798.

[21] Liu, Y., *et al.*, *Achievement of essentially full spatial coherence in a high-average-power soft-x-ray laser.* Physical Review A, 2001. **6303**(3).

[22] A. R. Libertun, X.Z., A. Paul, D. Raymondson, E. Greshgoren, E. Gagnon, S. Backus, M. M. Murnane, H. C. Kapteyn, R. A. Bartles, Y. Liu and D. T. Attwood. *High-resolution EUV*

imaging using high harmonic generation. in *Conference on Lasers and Electro-Optics Technical Digest.* 2004

[23] A. E. Yakshin, E.L., P. C. Gorts, E. L. G. Maas and F. Bijkerk, Determination of the Iayered structure on Mo/Si multilayers by grazing incidence X-ray reflectometry. Physica B, 2000. **283**: p. 143-148

[24] Anderson, E.H., Specialized Electron Beam Nanolithography for EUV and X-Ray Diffractive Optics. IEEE Journal of Quantum Electronics, 2006. **42**(1): p. 27-35.

[25] Anderson, E.H., *et al.*, "*Nanofabrication and diffractive optics for high-resolution x-ray applications".* Journal of Vacuum Science & Technology B, 2000. **18**(6): p. 2970-2975.

[26] R. W. Lee, S. J. Moon, H. K. Chung, W. Rozmus, H. A. Baldis, G. Gregori, R. C. Cauble, O. L. Landen, J. S. Wark, A. Ng, S. J. Rose, C. L. Lewis, D. Riley, J.-C. Gauthier, and P. Audebert. *Finite temperature dense matter studies on next-generation light sources*. J. Opt. Soc. Am. B 20, 770–778 (2003).

[27] M. Fajardo, P. Zeitoun, and J.-C. Gauthier. *Hydrodynamic simulation of XUV laser produced plasmas*. Eur. Phys. J. D 29, 69–75 (2004).

[28] B. R. Benware, A. Ozols, J. J. Rocca, I. A. Artioukov, V. V. Kondratenko, and A. V. Vinogradov. *Focusing of a tabletop soft-x-ray laser beam and laser ablation*. Opt. Lett. 24, 1714–1716 (1999).

[29] J. Dunn, Y. Li, A. L. Osterheld, J. Nilsen, J. R. Hunter, and V. N. Shlyaptsev, "Gain saturation regime for laser-driven tabletop, transient Ni-like ion x-ray lasers," Phys. Rev. Lett. 84, 4834–4837 (2000).

[30] K. A. Janulewicz, A. Lucianetti, G. Priebe, W. Sandner, and P. V. Nickles. *Saturated Ni-like Ag x-ray laser at 13.9 nm pumped by a single picosecond laser pulse.* Phys. Rev. A 68, 051802 (2003).

[31] Y. Wang, M. A. Larotonda, B. M. Luther, D. Alessi, M. Berrill, V. N. Shlyaptsev, and J. J. Rocca. *Demonstration of high-repetition-rate tabletop soft-x-ray lasers with saturated output at wavelengths down to 13.9 nm and gain down to 10.9 nm.* Phys. Rev. A 72, 053807 (2005).

[32] M. A. Larotonda, Y. Wang, M. Berrill, B. M. Luther, J. J. Rocca, M. M. Shakya, S. Gilbertson, and Z. Chang. *Pulse duration measurements of grazing incidence pumped high repetition rate Ni-like Ag and Cd transient soft-x-ray lasers.* Opt. Lett. 31, 3043–3045 (2006).

[33] Ph. Zeitoun, G. Faivre, S. Sebban, T. Mocek, A. Hallou, M. Fajardo, D. Aubert, Ph. Balcou, F. Burgy, D. Douillet, S. Kazamias, G. de Lachèze-Murel, T. Lefrou, S. le Pape, P. Mercère, H. Merdji, A. S. Morlens, J. P. Rousseau, and C. Valentin. *A high-intensity highly coherent soft x-ray femtosecond laser seeded by a high harmonic beam.* Nature 431, 426–429 (2004).

[34] Y. Wang, E. Granados, M. A. Larotonda, M. Berrill, B. M. Luther, D. Patel, C. S. Menoni, and J. J. Rocca. *High- brightness injection-seeded soft-x-ray-laser amplifier using a solid target*. Phys. Rev. A 22, 123901 (2006).

[35] Y. Wang, E. Granados, F. Pedaci, D. Alessi, B. Luther, M. Berrill, and J. J. Rocca. *Phase-coherent, injection-seeded, table-top soft-x-ray lasers at 18.9 nm and 13.9 nm*. Nat. Photonics 2, 94–98 (2008).

[36] M. Grisham, G. Vaschenko, C. S. Menoni, J. J. Rocca, Yu. P Pershyn, E. N. Zubarev, D. L. Voronov, V. A. Sevryukova, V V. Kondratenko, A. V. Vinigradov, and I. A. Artioukov. *Damage to extreme-ultraviolet Sc/Si multilayer mirrors exposed to intense 46.9-nm laser pulses*. Opt. Lett. 29, 620–622 (2004).

[37] L. Juha, M. Bittner, D. Chvostova, V. Letal, J. Krasa, Z. Otcenasek, M. Kozlova, J. Polan, A. R. Präg, B. Rus, M. Stupka, J. Krzywinski, A. Andrejczuk, J. B. Pelka, R. Sobierajski, L. Ryc, J. Feldhaus, F. P. Boody, M. E. Grisham, G. O. Vaschenko, C. S. Menoni, and J. J. Rocca. *XUV-laser induced ablation of PMMA with nano-, pico-, and femtosecond pulses*. J. Electron Spectrosc. Relat. Phenom. 144, 929–932 (2005).

[38] M. Bittner, L. Juha, B. Rus, M. Kozlova, J. Krasa, Z. Otcenasek, J. Polan, A. R. Praeg, M. Stupka, L. Ryc, and R. H. Sobierajski. *Material ablation induced by focused 21.2- nm radiation from Ne-like Zn x-ray laser*. Proc. SPIE 5777, 965–969 (2005).

[39] T. Mocek, B. Rus, M. Stupka, M. Kozlová, A. R. Präg, J. Polan, M. Bittner, R. Sobierajski, and L. Juha. *Focusing a multimillijoule soft x-ray laser at 21 nm*. Appl. Phys. Lett. 89, 051501 (2006).

[40] J. J. Rocca, V. Shlyaptsev, F. G. Tomasel, O. D. Cortázar, D. Hartshorn, and J. L. A. Chilla. *Demonstration of a discharge pumped table-top soft-x-ray laser*. Phys. Rev Lett. 73, 002192 (1994).

[41] B. R. Benware, C. D. Macchietto, C. H. Moreno, and J. J. Rocca. *Demonstration of a high average power tabletop soft x-ray laser*. Phys. Rev. Lett. 81, 5804–5807 (1998).

[42] Yu. A. Uspenskii, V. E. Lebashov, A. V. Vinogradov, A. I. Fedorenko, V. V. Kondratenko, Yu. P. Pershin, E. N. Zubalev, and V. Yu. Fedotov. *High-reflectivity multilayer mirrors for a vacuum-ultraviolet interval of 35–50 nm*. Opt. Lett. 23, 771–773 (1998).

[43] M. A. Berrill. *A computer model to simulate laser created plasmas used for the generation of extreme ultraviolet light*. M.S. thesis (Colorado State University, 2006).

[44] G. J. Pert. *The hybrid model and its application for studying free expansion*. J. Fluid Mech. 131, 401–426 (1983).

[45] M. F. Hu. *Indirect x-ray line-formation processes in iron L-shell ions*. Astrophys. J. 582, 1241–1250 (2003).

[46] R. F. Reilman and S. T. Manson. *Photoabsorption cross sections for positive atomic ions with 30≥Z.* Astrophys. J., Suppl. Ser. 40, 815–880 (1979).

[47] NIST Atomic Spectra Database Version 3, http://physics.nist.gov/PhysRefData/ASD/index.html.